The Global Ocean Water Cycle in Atmospheric Reanalysis, Satellite, and Ocean Salinity

LISAN YU,[a] XIANGZE JIN,[a] SIMON A. JOSEY,[b] TONG LEE,[c] ARUN KUMAR,[d] CAIHONG WEN,[d,e] AND YAN XUE[d]

[a] *Woods Hole Oceanographic Institution, Woods Hole, Massachusetts*
[b] *National Oceanography Centre, Southampton, United Kingdom*
[c] *Jet Propulsion Laboratory, California Institute of Technology, Pasadena, California*
[d] *Climate Prediction Center, NCEP/NWS/NOAA, College Park, Maryland*
[e] *Innovim, Greenbelt, Maryland*

(Manuscript received 28 June 2016, in final form 4 January 2017)

ABSTRACT

This study provides an assessment of the uncertainty in ocean surface (OS) freshwater budgets and variability using evaporation E and precipitation P from 10 atmospheric reanalyses, two combined satellite-based $E - P$ products, and two observation-based salinity products. Three issues are examined: the uncertainty level in the OS freshwater budget in atmospheric reanalyses, the uncertainty structure and association with the global ocean wet/dry zones, and the potential of salinity in ascribing the uncertainty in $E - P$. The products agree on the global mean pattern but differ considerably in magnitude. The OS freshwater budgets are 129 ± 10 (8%) cm yr^{-1} for E, 118 ± 11 (9%) cm yr^{-1} for P, and 11 ± 4 (36%) cm yr^{-1} for $E - P$, where the mean and error represent the ensemble mean and one standard deviation of the ensemble spread. The $E - P$ uncertainty exceeds the uncertainty in E and P by a factor of 4 or more. The large uncertainty is attributed to P in the tropical wet zone. Most reanalyses tend to produce a wider tropical rainband when compared to satellite products, with the exception of two recent reanalyses that implement an observation-based correction for the model-generated P over land. The disparity in the width and the extent of seasonal migrations of the tropical wet zone causes a large spread in P, implying that the tropical moist physics and the realism of tropical rainfall remain a key challenge. Satellite salinity appears feasible to evaluate the fidelity of $E - P$ variability in three tropical areas, where the uncertainty diagnosis has a global indication.

1. Introduction

Over the open ocean away from the influence of continental runoffs and sea ice, the freshwater content is the residual of ocean surface (OS) evaporation E and precipitation P. On an annual basis, ocean E and P are not balanced. The ocean produces about 87% of the global (ocean and land) evaporation and receives only 78% of the global precipitation (Baumgartner and Reichel 1975). The imbalance implies that there is a net transport of water from the ocean to the continents through the atmosphere, making the ocean an important, albeit remote, source of continental precipitation (Trenberth et al. 2011; Gimeno et al. 2012; van der Ent and Savenije 2013). The need for a valid and reliable tool to better estimate the changing oceanic freshwater balance and its impact on the oceanic moisture supply to the terrestrial water cycle is well recognized (Rhein et al. 2013; Hegerl et al. 2015). The state-of-the-art global atmospheric reanalyses, which provide quantitative estimates of the global hydrological cycle, are regarded as a potentially useful tool to address the need (e.g., Trenberth et al. 2007; Bosilovich et al. 2011; Lorenz and Kunstmann 2012). From an oceanographic perspective, the E-minus-P (hereinafter $E - P$) flux is a surface freshwater flux forcing of the ocean, which, together with ocean dynamics, drives the spatial and temporal changes of ocean salinity, influencing water mass formation and ocean circulation as well as mediating air–sea interaction (Dickson et al. 1988; Lukas and Lindstrom 1991). Observations have revealed significant trends in ocean salinity in the past decades (e.g., Dickson et al. 1988; Terray et al. 2012). The long-term time series provided by the retrospective analyses from atmospheric models are potential tools for putting ocean salinity observations into context.

Corresponding author e-mail: Dr. Lisan Yu, lyu@whoi.edu

DOI: 10.1175/JCLI-D-16-0479.1

Atmospheric reanalysis (or retrospective analysis) uses sequential data assimilation methods to combine observations with model dynamics to produce the atmospheric state of past decades (Trenberth and Olson 1988). Recent efforts have also been made to extend the reanalysis period to the twentieth century and earlier (Compo et al. 2011). To date, the progression of reanalysis efforts can be categorized into three generations, each with better spatial and temporal resolutions and more refined model parameterization schemes and data assimilation systems. The most widely used reanalyses in the first generation are the Reanalysis 1 from the National Oceanic and Atmospheric Administration (NOAA) National Centers for Environmental Prediction (NCEP) and the National Center for Atmospheric Research (NCAR) (hereafter NCEP1; Kalnay et al. 1996), and the Reanalysis 2 from NCEP and the Department of Energy (DOE) (hereafter NCEP2; Kanamitsu et al. 2002). The most representative reanalysis for the second generation is the European Centre for Medium-Range Weather Forecasts (ECMWF) 40-Year Re-Analysis (ERA-40; (Uppala et al. 2005). The third generation currently has four products: the Climate Forecast System Reanalysis (CFSR) from NCEP (Saha et al. 2010), the ECMWF interim reanalysis (ERA-Interim; Dee et al. 2011), the Modern-Era Retrospective Analysis for Research and Applications (MERRA) from the National Aeronautics and Space Administration (NASA) (Rienecker et al. 2011), and the Japanese Meteorological Agency (JMA) 55-Year Reanalysis (JRA-55; Kobayashi et al. 2015). In addition, the twentieth-century reanalysis efforts have led to two products, the Twentieth Century Reanalysis Project (20CR; Compo et al. 2011) and the ECMWF twentieth-century reanalysis (ERA-20C; (Hersbach et al. 2015). The most recent release in the continuing reanalysis efforts is the second version of MERRA (MERRA-2; Molod et al. 2015). A summary of the general specifications of the 10 reanalyses is listed in Table 1.

Reanalysis products are known to have large uncertainties. Some of the biases originate from data assimilation, parameterizations, or treatments of subgrid/small-scale physical processes, and physical assumptions in the model. Others are due to changes in observation systems (e.g., the introduction of data from a new satellite to the data assimilation system or decommission of a satellite), which often lead to erroneous spatial and temporal changes of the estimated atmospheric state. For instance, artificial jumps and trends in time series and localized spatial anomalies have been reported in reanalyzed freshwater and heat flux fields (Bengtsson et al. 2004; Bosilovich et al. 2008; Zhang et al. 2012; Josey et al. 2014). In 2013, NOAA established a Climate Reanalysis Task Force (CRTF) to focus on researching reanalysis improvements and outstanding issues. The uncertainty of the energy and freshwater budgets over the global ocean was identified as one of seven main research topics (Compo et al. 2016). The present study reports the effort on evaluating the ocean-surface freshwater budgets and uncertainties under the auspices of the CRTF activities.

Various metrics have been applied to assess the uncertainties in the reanalyzed E and P. Satellite-based P products, such as the Global Precipitation Climatology Project (GPCP) (Huffman et al. 1997; Adler et al. 2003) and the Climate Prediction Center (CPC) Merged Analysis of Precipitation (CMAP) monthly precipitation dataset (Xie and Arkin 1997), have been commonly used to evaluate the reanalysis products. There are studies that used satellite P products to examine the mean P products in terms of geographical distributions and zonally averaged means to highlight the differences in magnitude (e.g., Roads 2003; Kumar et al. 2004; Quartly et al. 2007). There are studies that employed statistical approaches, such as spatial/temporal correlations and the empirical orthogonal function (EOF) analysis to characterize the differences in spatial patterns (e.g., Janowiak et al. 1998; Bosilovich et al. 2008). There are studies that combined the ocean $E - P$ budget with the terrestrial P from observations and E estimates from land surface models (e.g., Mueller et al. 2013) to check the freshwater balance and associated uncertainties on the global scale (e.g., Schlosser and Houser 2007; Lorenz and Kunstmann 2012). However, differences between GPCP and CMAP over the ocean are noted, particularly in the tropical and high latitudes (Yin et al. 2004). These differences are attributed largely to the inclusion of in situ rain gauge measurements and to the technical limitations in retrieving snowfall and cold-season P. To overcome the uncertainties associated with satellite P products, dynamically based metrics, such as the atmospheric conservation of moisture, are introduced to relate $E - P$ to vertically integrated moisture convergence (Trenberth et al. 2011; Robertson et al. 2014). This type of approach is deemed more reliable, as it allows the fidelity of $E - P$ produced by model physics to be evaluated by analyzed state variables of wind and moisture.

Using ocean state variables (temperature and salinity) as a diagnostic tool for the ocean water cycle has received great attention in recent decades because of the need to better understand the ocean as the largest reservoir of freshwater and the need to improve the utilization of the rapidly augmented ocean salinity database from satellite and in situ observing platforms. The $E - P$

TABLE 1. List of the *E*, *P*, and salinity products and their associated main characteristics.

Name	Source	Period	Available temporal resolution	Available spatial resolution	Model resolution	Assimilation scheme	Reference
Atmospheric reanalyses (*E* and *P*)							
NCEP1	NCEP, NCAR	1948 onward	6 hourly	1.875° × 1.875°	T62, 28 levels	3DVAR	Kalnay et al. (1996)
NCEP2	NCEP, DOE	1979 onward	6 hourly	1.875° × 1.875°	T62, 28 levels	3DVAR	Kanamitsu et al. (2002)
CFSR	NCEP	1979 onward	Hourly	0.5° × 0.5°	T382, 64 levels	3DVAR	Saha et al. (2010)
ERA-40	ECMWF	1957–2002	6 hourly	1.125° × 1.125°	T159, 60 levels	3DVAR	Uppala et al. (2005)
ERA-Interim	ECMWF	1979 onward	6 hourly	0.7° × 0.7°	T255, 60 levels	4DVAR	Dee et al. (2011)
ERA-20C	ECMWF	1900–2010	3 hourly	1.125° × 1.125°	T159, 37 levels	4DVAR	Poli et al. (2013)
MERRA	NASA	1979 onward	3 hourly	0.667° × 0.5°	Cubed sphere grid, 72 levels	3DVAR	Rienecker et al. (2011)
MERRA-2	NASA	1980 onward	Hourly	0.625° × 0.5°	Cubed sphere grid, 72 levels	3DVAR	Molod et al. (2015)
JRA-55	JMA	1958 onward	3 hourly	0.55° × 0.55°	T319, 60 levels	4DVAR	Kobayashi et al. (2015)
20CR (v2c)	NOAA/ESRL/CIRES/CDC	1950 to 2011	6 hourly	2° × 2°	T62, 28 levels	3DVAR	Compo et al. (2011)
Name	Source	Period	Temporal Resolution	Spatial Resolution	Variable	Analysis Scheme	Reference
Satellite-based *E* and *P* products							
OAFlux	WHOI	1958/01 onward	Daily	1° × 1°	*E*	Objective synthesis	Yu et al. (2008)
GPCP	NASA	1979/01 onward	Daily	2.5° × 2.5°	*P*	Multisensor merging	Adler et al. (2003)
CMAP	NOAA	1979/01 onward	Daily	2.5° × 2.5°	*P*	Multisensor merging	Xie and Arkin. (1997)
Ocean salinity datasets							
Aquarius	JPL	June 2011–June 2015	Monthly	1° × 1°	Satellite SSS	Combined active-passive	Yueh et al. (2014)
Argo	JAMSTEC	2003 onward	Monthly	1° × 1°	In situ SSS	Optimal interpolation	Hosoda et al. (2010)

flux is a forcing of ocean salinity, and the change of the ocean water cycle should be reflected in ocean salinity (Elliott 1974; Terray et al. 2012). Evaluating the $E - P$ products based on the vertically integrated salt conservation equation has been investigated by several studies (e.g., Yu 2011; Vinogradova and Ponte 2013). Ren et al. (2014) and Giglio and Roemmich (2014) used Argo salinity observations to examine the E and P products. Schanze et al. (2010) computed the closure of the ocean water budget between E, P, and runoff R and found that the budget closes within the errors estimates of the three products in use, that is, E from the Objectively Analyzed Air–Sea Fluxes (OAFlux) (Yu and Weller 2007; Yu et al. 2008), P from GPCP (Huffman et al. 1997; Adler et al. 2003), and R from Dai et al. (2009). Given the value of ocean salinity as an independent source of verification of the ocean water cycle, our evaluation effort that was made to support the NOAA CRTF activities has one specific task in mind: to determine to what degree the fidelity of the E and P products can be assessed by ocean salinity observations.

Hence, the objectives of this study are twofold: to provide an up-to-date quantification of the ocean–surface freshwater budget and uncertainties, and to test the applicability of ocean salinity as a tool for validating the $E - P$ estimates. A total of 12 $E - P$ products are examined, which include 10 reanalyses (i.e., NCEP1, NCEP2, ERA-40, CFSR, ERA-Interim, JRA-55, MERRA, MERRA-2, ERA-20C, and 20CR) and two satellite-based combined $E - P$ products (i.e., OAFlux-GPCP and OAFlux-CMAP). Two sets of salinity observations are also explored. Section 2 provides a description of the datasets, and section 3 presents the analysis results. Key findings are summarized in section 4.

2. Data description

a. *The* E − P *reanalysis products*

Major features of the 12 $E - P$ products are summarized in Table 1. The NCEP1, ERA-40, and JRA-55 archives start from the late 1950s and rely on conventional, sparse, and irregularly distributed in situ observations for the presatellite period. The NCEP2, CFSR, ERA-Interim, MERRA, and MERRA-2 reanalyses focus on the modern satellite era from 1979 (or 1980 for MERRA-2) onward to capitalize on the rapidly increasing volume of satellite observations (note that NCEP1, ERA-40, and JRA-55 also make use of this data in the satellite period). The two twentieth-century reanalyses have more than 100 years of time series: 20CR covers the period from 1870 to 2011, and ERA-20C from 1900 to 2010. They assimilate only surface information to avoid artificial changes in the state estimation due to changes in the atmospheric observing systems. 20CR employed surface pressure and sea surface temperature (SST) (Compo et al. 2011) and ERA-20C used surface pressure and surface marine winds (Poli et al. 2013). CFSR is the only reanalysis that features a weakly coupled atmosphere–ocean–land reanalysis; all the other reanalyses are atmospheric-only reanalyses in which the atmospheric state is forced by the imposed SST boundary conditions at the ocean surface. The inclusion of weakly coupled data assimilation in CFSR has a potential for better depiction of the overall atmosphere–ocean feedback processes than the uncoupled data assimilations (Wen et al. 2012; Kumar and Hu 2012; Jin and Yu 2013).

The 35-yr satellite period from January 1979 to December 2014 is taken as the analysis period for this study, in the expectation that satellite observations would provide a better constraint to the reanalysis of the state of the atmospheric system and, consequently, a better estimate of the freshwater cycle over the ocean. Three reanalyses do not have the full 35-yr coverage. They are ERA-40 (up to August 2002), 20CR (up to December 2011), and ERA-20C (up to December 2010). For these three products, the mean climatology was constructed from the respective maximum duration of the period in study. All products were regridded to the $1° \times 1°$ grids for comparison.

b. *Satellite* E − P *products*

The GPCP (Huffman et al. 1997; Adler et al. 2003) and CMAP (Xie and Arkin 1997) monthly P datasets are developed from blending rain gauge measurements with satellite P estimates from various sensors, including passive microwave imagers, visible and infrared radiances on geostationary satellites, and precipitation radars, and are available from 1979 to the present on $2.5° \times 2.5°$ grids. This study uses the GPCP version 2.2 (Huffman et al. 2009) and the observation-only CMAP analysis (Xie and Arkin 1997). Yin et al. (2004) showed that the two products differ in the detailed merging techniques, particularly regarding the method of merging the satellite and rain gauge data, and the use of atoll data in CMAP is questionable. Differences in P estimates are evident in the tropical and high-latitude oceans, and the decadal trend of the CMAP P appears to be erroneous over the ocean.

OAFlux E is computed from the bulk flux parameterization of Fairall et al. (2003) using flux-related variables (such as wind speed, SST, near-surface air humidity, and temperature) as input. Except for SST, which is taken from the Optimum Interpolation SST (Reynolds et al. 2007), all other variables are derived

TABLE 2. Global ocean-surface budgets (cm yr^{-1}) of E, P, $E - P$, and related ratios constructed from E and P. (Note that ERA-40 is not included in the computation of ensemble mean and spread.)

Name	E	P	$E - P$	E/P	$[(E - P)/E] \times 100$ (%)
NCEP1	120	110	10	1.1	8
NCEP2	137	130	7	1.0	5
CFSR	132	128	4	1.0	3
ERA-40	128	132	−4	1.0	−3
ERA-Interim	128	118	10	1.1	8
ERA-20C	130	121	9	1.1	7
MERRA	115	104	11	1.1	10
MERRA-2	133	112	21	1.2	16
JRA-55	146	134	12	1.1	8
20CR	139	124	15	1.1	11
OAFlux-GPCP	118	107	11	1.1	9
OAFlux-CMAP	118	106	12	1.1	10
Ensemble mean	129	118	11	1.1	9
STD [(STD/mean) × 100%]	10 (8%)	11 (9%)	4 (36%)	0.05 (5%)	3 (38%)

from satellite observations. Wind speed is from the recent OAFlux vector wind analysis that is merged from 16 satellite sensors (Yu and Jin 2014a,b), and the near-surface air temperature and humidity are an objective synthesis of satellite products (Jin et al. 2015). The version used in this study is an update of the version previously published (Yu and Weller 2007). Studies have shown that the combined $E - P$ from OAFlux and GPCP produces a freshwater budget that is best consistent with the ocean salt content (Schanze et al. 2010; Ren et al. 2014) and the atmospheric moisture content (Robertson et al. 2014) among the products chosen for evaluation. The authors in this study are aware of several other satellite-based E and P products. Since this study was under the auspices of the NOAA CRTF activities that focused on the ocean water cycle in atmospheric reanalysis, intercomparison of satellite-based products is beyond the scope.

c. *Ocean salinity observations*

Two sets of salinity observations are used (Table 2): the sea surface salinity (SSS) from the NASA's *Aquarius*/*SAC-D* mission and the subsurface salinity fields from Argo. The *Aquarius* satellite on board the *SAC-D* spacecraft was a combined passive/active L-band microwave radiometer/radar instrument that was launched on 11 June 2011 (Lagerloef et al. 2008) but ended on 8 June 2015 due to power failure. The mission yielded a total of three years and nine months of valuable SSS observations. The *Aquarius* SSS product used here is the Level-3 Combined Active-Passive (CAP) version 4.0 product (Yueh et al. 2014).

The Argo monthly gridded data product is produced by the Japan Agency for Marine-Earth Science and Technology (JAMSTEC) (Hosoda et al. 2010) from optimal interpolation (OI) of Argo floats, Triangle Trans-Ocean Buoy Network (TRITON), and available conductivity–temperature–depth (CTD) casts. The salinity fields are gridded onto 1° grids horizontally, and 25 pressure levels from 2000 to 10 dbar below the surface. We used the salinity of the surface mixed layer rather than the salinity at 5 db when comparing with the *Aquarius* SSS. The mixed-layer depth h was determined as the depth at which the density below the depth of 10 dbar is 0.125 kg m^{-3} higher than the surface density (de Boyer Montégut et al. 2004). To be consistent, the 3-yr record from January 2012 to December 2014 (i.e., the three complete calendar years that are available for the *Aquarius* record) was used to construct the mean seasonal cycle for both Argo and *Aquarius*.

3. Analysis

a. *Ensemble* E − P *mean and spread*

Ensemble mean and spread are commonly used statistical properties to quantify the degree of discrepancy between ensemble members. Ensemble mean fields of E, P, and $E - P$ consisting of all 12 products were constructed (Figs. 1a–c). Three patterns characterize the large-scale spatial distribution of the ocean $E - P$: 1) the tropical wet zone between about 15°S and 15°N, where P dominates E due to the intense rainfall associated with the ITCZ and the South Pacific convergence zone (SPCZ), 2) the subtropical dry zones between 15° and 40° north and south of the equator, where E dominates P along the subtropical high pressure belts, and 3) the subpolar wet (i.e., P dominant) zones between 40° and 60° north and south, as a result of the influence of the midlatitude storm tracks. Note that a sea ice mask was applied to all products because satellite retrievals of flux-related variables (wind speed, SST, air temperature,

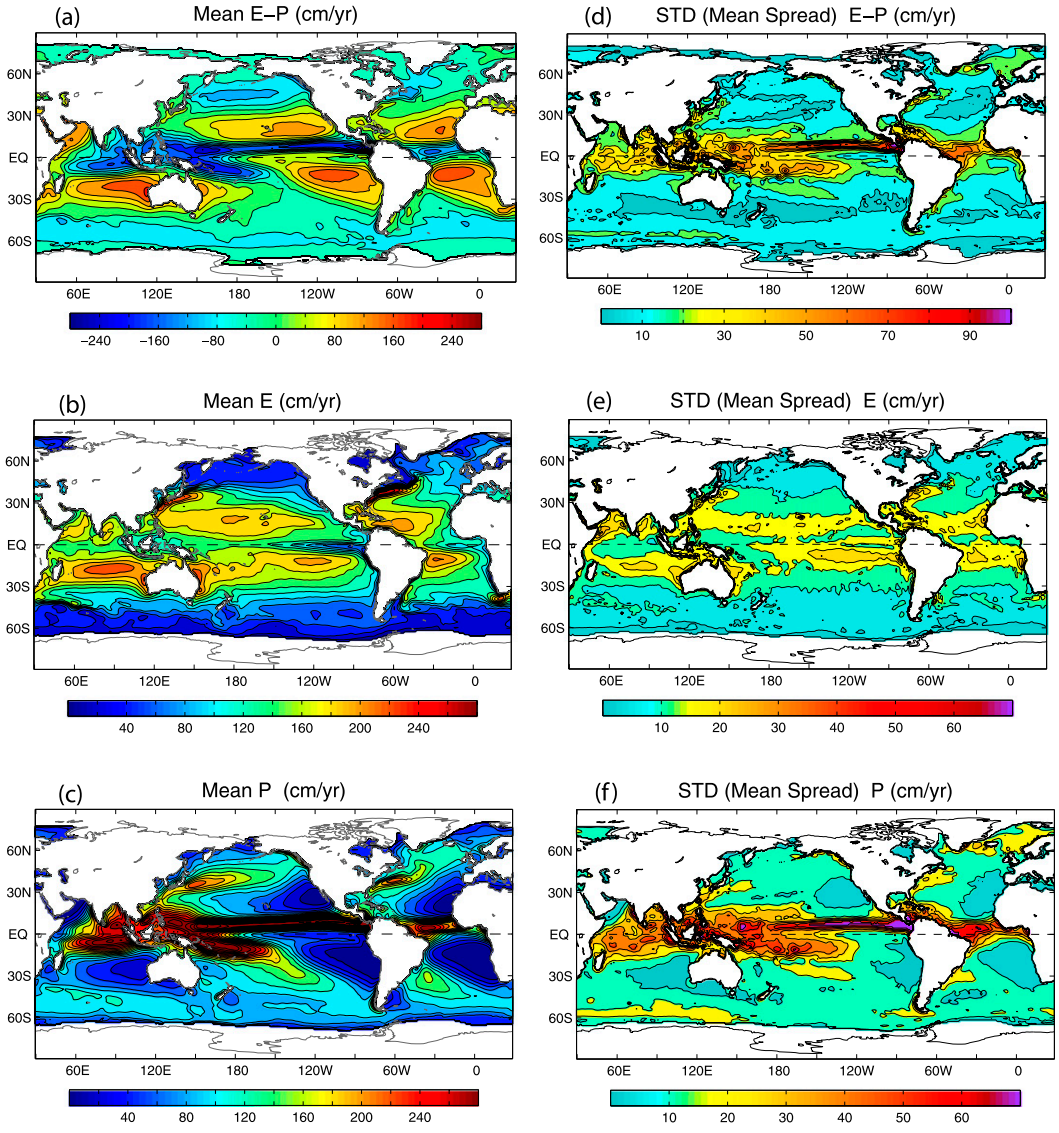

FIG. 1. Ensemble mean of (a) E, (b) P, and (c) $E - P$ constructed from 12 $E - P$ products, and STD of the spread between the 12 products in (d) E, (e) P, and (f) $E - P$.

and humidity) do not have values over the ice-covered regions. The sea ice mask was derived from the National Snow and Ice data Center (NSIDC) based on a 50% sea ice concentration threshold (Yu et al. 2008).

Despite the similarities in the spatial distribution, the 12 products differ considerably in magnitude. The spread in the mean is represented here by the standard deviation (STD) between the products (Figs. 1d–f). The spread in $E - P$ is most pronounced in the tropical/subtropical regions between 40°S and 40°N, dominated by the spread in P in regions of the ITCZ and SPCZ. The zonal averages of the ensemble mean and spread (Figs. 2a–c) show that the spread in the products is proportional to the magnitude of the mean values. The spread in P is largest in the rainy tropical wet zone, whereas the spread in E is largest in the evaporative subtropical dry zone.

Large (small) spread indicates a low (high) confidence in the E and P estimates. If normalizing the spread by the mean (Figs. 2d–f), the ratio, denoted by σ, would be a good measure of the uncertainty level in the present E and P estimates. The ratio is a strong function of latitude. Note that $\sigma(E)$ is held near the 10% uncertainty level in the low-to-middle latitudes (40°S–50°N) but increases sharply to near the 30% level (Fig. 2e) when approaching higher latitudes. By comparison, $\sigma(P)$ is much higher. Except for the latitudes near 40°N/S where $\sigma(P)$ is lowest at 12%, $\sigma(P)$ is about 25% in the tropical wet zone and 30% and greater at higher-latitude wet zones. The

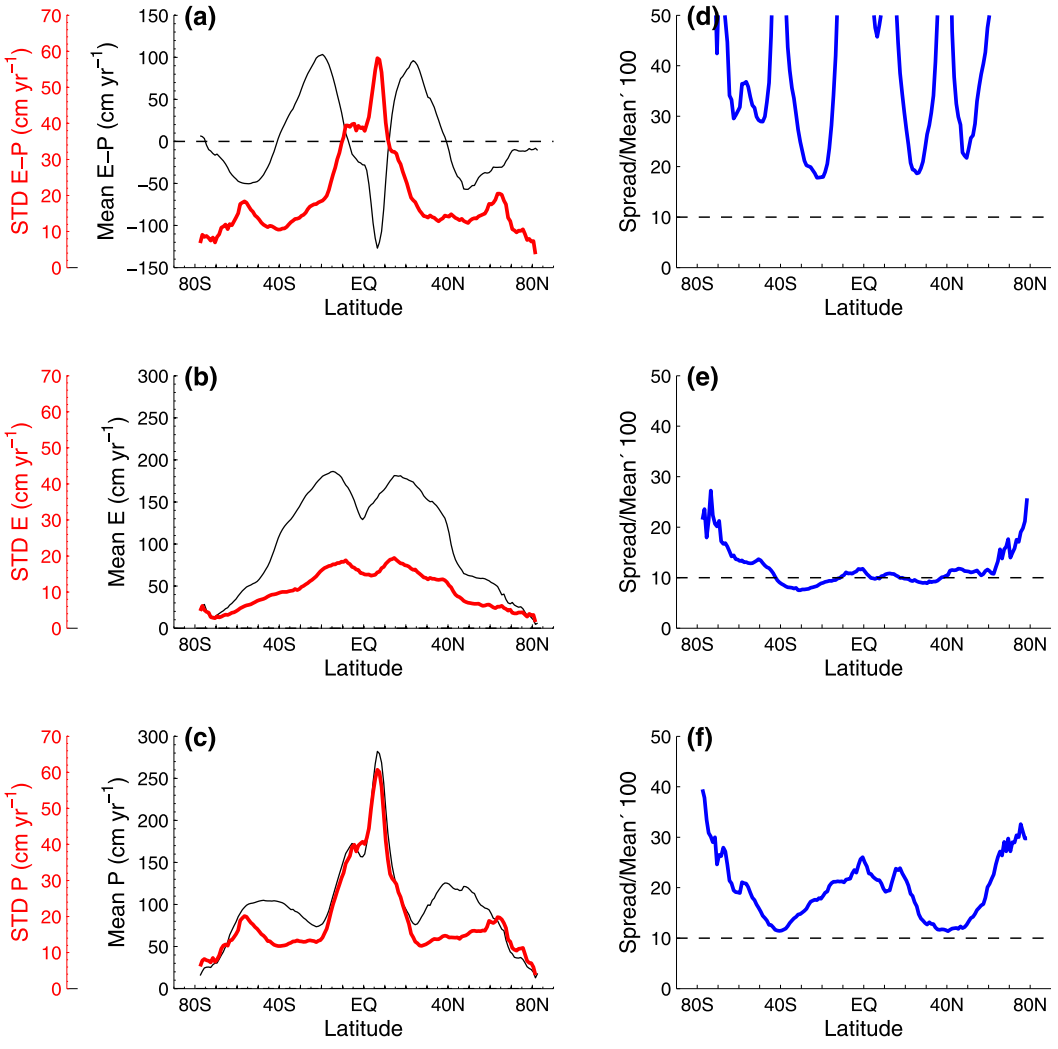

FIG. 2. Zonal mean average of the ensemble mean (black) vs the ensemble spread (red) in (a) $E - P$, (b) E, and (c) P, and the percentage of the ensemble spread/mean in (d) $E - P$, (e) E, and (f) P.

uncertainty level in $E - P$ is even greater. The value of $\sigma(E - P)$ is seen to be above 25% across all latitudes.

An accuracy goal of 10% or better has been set for the gridded flux products (Taylor et al. 1999). While the E products in the low-to-middle latitudes meet the accuracy requirement, the P products are far from the required level, and the $E - P$ products are nowhere near. The σ values indicate that more accurate representations of the tropical P as well as improved E and P estimates at high latitudes are key for improving the ocean-surface freshwater budgets.

b. *Internal relationships between* E, P, *and* E − P *budgets*

The global-ocean averaged budgets for $E - P$ differ considerably between products (Fig. 3a), ranging from 4 cm yr^{-1} (CFSR) to 21 cm yr^{-1} (MERRA-2), with ERA-40 producing the only negative $E - P$ budget. ERA-40 is obviously erroneous, since the ocean is the source of atmospheric moisture (e.g., Gimeno et al. 2012) and the global ocean average of $E - P$ should not be negative. Hagemann et al. (2005) reported that the biases in the global water budget in ERA-40 are strongly influenced by the introduction of satellite observations in late 1980s, causing excessive moistening and, consequently, excessive rainfall in the tropical ocean. ERA-40 is thus excluded in the following ensemble-mean based calculations (Table 2). The mean budget generated from the remaining 11 products is on the order of 129 ± 10 (8%) cm yr^{-1} for E and 118 ± 11 (9%) cm yr^{-1} for P, where the error bar is the STD of the ensemble spread. The ensemble mean of $E - P$ budget is on the order of 11 ± 4 (36%) cm yr^{-1}.

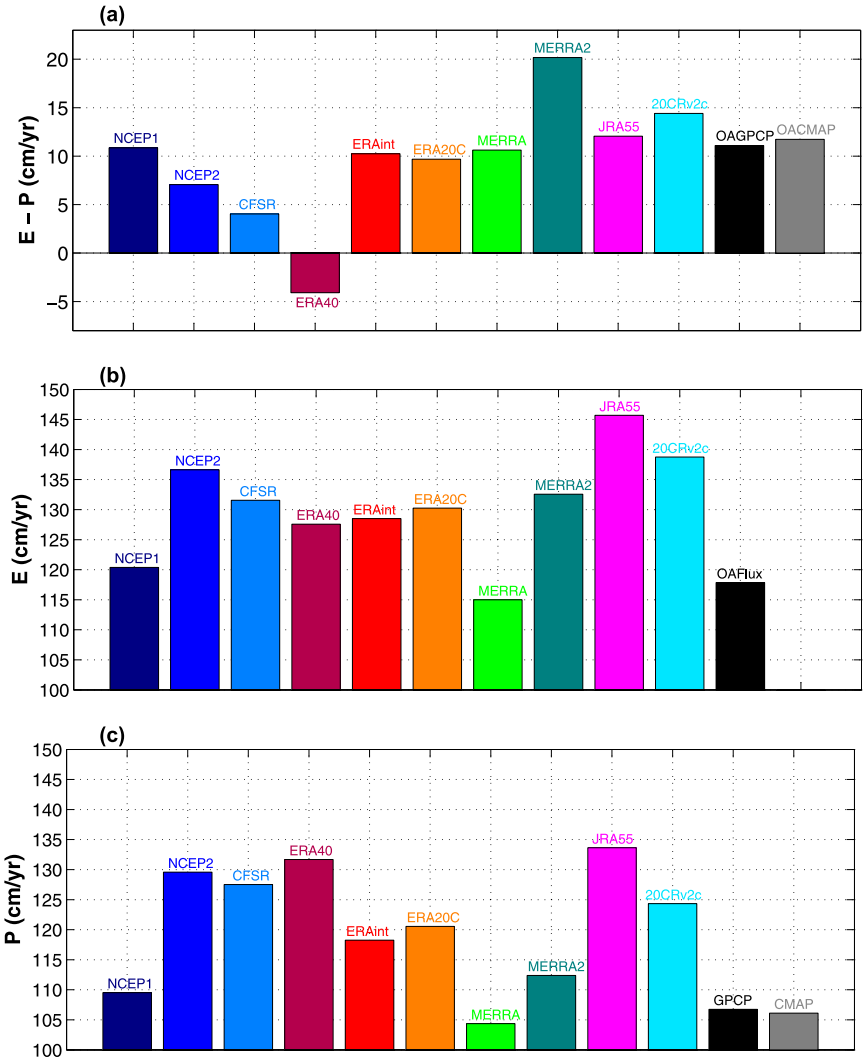

FIG. 3. Global ocean-surface mean average of (a) $E - P$, (b) E, and (c) P.

MERRA produces the weakest budget in both E (114 cm yr^{-1}) and P (104 cm yr^{-1}), while JRA-55 has the largest budget in both E (145 cm yr^{-1}) and P (133 cm yr^{-1}). However, it is neither MERRA nor JRA-55 but MERRA-2 that tops the total $E - P$ budgets (Fig. 3a and Table 2). Clearly, the global-ocean $E - P$ budget does not depend on individual E or P. Examining all the 12 products, MERRA-2 has E and P out of proportion: the E budget is on the lower end while the P budget is on the higher end. The E and P budgets in ERA-40 are also not in proportion, as the P budget is on the higher end and the E budget is in the median range so that its $E - P$ is erroneously negative. This leads to the question as to what the E/P ratio means in balancing the global-ocean $E - P$ budget. Here the E/P ratio was computed (Fig. 4a; Table 2), showing that four products (MERRA, OAFlux-CMAP, OAFux-GPCP, and NCEP1) have an E/P ratio of 1.1 and four products (ERA-Interim, ERA-20C, 20CRv2c, and JRA-55) have a ratio close to 1.1. However, three products (NCEP2, CFSR, and ERA-40) have a low E/P ratio of 1.0, and MERRA-2 has a high ratio of 1.2. The ratio based on the ensemble mean estimates of E (129 cm yr^{-1}) and P (118 cm yr^{-1}) is 1.1.

On the annual-mean basis, the total freshwater budget over the global ocean should be balanced, that is $E - P - R \approx 0$, where R denotes river runoff (because variations in water storage on land means that this balance is not precisely zero). If expressing E/P in terms of $E/P \approx (P + R)/P = 1 + R/P$, one can see that the larger (smaller) the ratio, the more (less) continental runoff is needed to balance the water budget over the ocean. Hence, the E/P ratio measures the relative strength of ocean mean evaporation to the amount of rainfall that comes back to the ocean. A large value requires a

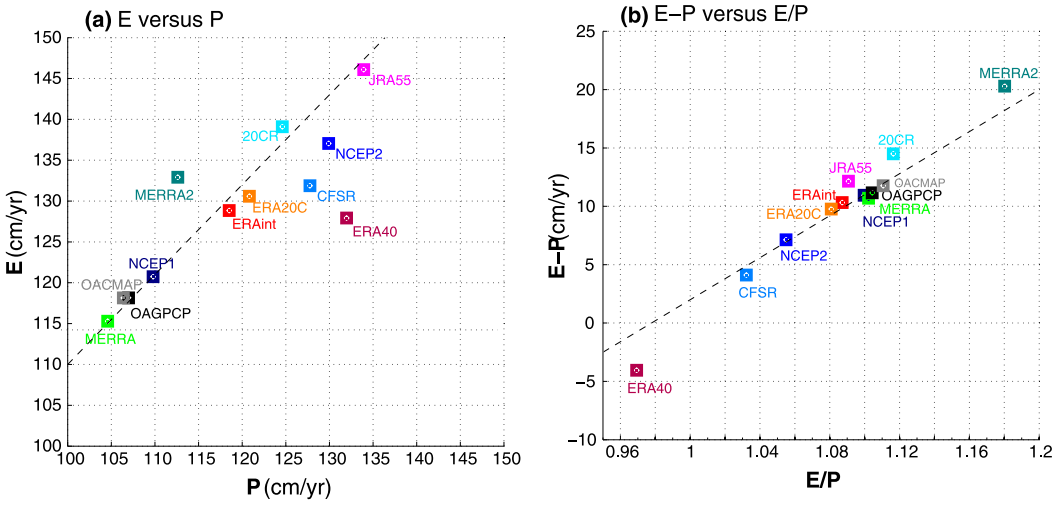

FIG. 4. (a) The ratio of the global ocean-surface mean average of E to P. The black dashed line denotes that the E/P ratio equals to 1.10. (b) The ratio of the global ocean-surface mean average of $E - P$ to E/P. The dashed line denotes the best fit.

proportionately greater return from river runoff to balance the large evaporation from the ocean.

The efficiency of the ocean as a moisture source to terrestrial rainfall can be represented by the percentage ratio of $[(E - P)/E] \times 100\%$. The reanalyses vary from a low of 3%–5% (CFSR and NCEP2) to a high of 16% (MERRA-2). The efficiency ratio for the remaining nine products ranges between 7% and 11%. The ensemble-mean based calculation is 9%.

c. *How is mass balanced in reanalysis?*

The large spread in the reanalyzed $E - P$ budget reflects the fact that the atmospheric physics in models does not include atmospheric water in mass budget (with the exception of MERRA-2). Mass changes due to water content are implicitly treated in the surface pressure analysis, as the effects of these changes are assumed to be included in surface pressure observations (Bosilovich et al. 2015, 2016). Since no overall hydrological balance is imposed, the water budget is not required to be in complete balance. The surface P in most reanalyses is generated by the atmospheric modeling component of the system, following the assimilation of atmospheric temperature and humidity observations that come from several sources, including humidity profiles from radiosondes and satellite microwave radiances. During each analysis cycle, the assimilation scheme tries to add or remove moisture (and hence water) by adjusting the model atmosphere to fit the observations. This leads to an analysis that is close to observations but not necessarily in balance with the model's own state of vapor climate (Trenberth and Smith 2005). However, models such as MERRRA and MERRA-2 include an analysis increment in the budget to enforce the moisture budget closure. In addition, MERRA-2 constrains the global dry atmospheric mass to be constant while total mass and moisture changes are consistent with $E - P$.

The most recent reanalyses, such as CFSR and MERRA-2, implemented the correction of the model-generated precipitation over land using merged satellite/gauge-based precipitation observation products [e.g., the GPCP, CMAP, and the CPC Unified Gauge-Based Analysis of Global Daily Precipitation (CPCU; Chen and Xie 2008)] (Saha et al. 2010; Bosilovich et al. 2015). The models included also analysis increment to enforce the moisture budget closure.

d. *Mean* E − P *structure and uncertainty*

The zonal averages of the time-mean $E - P$ fields from the 12 products (Fig. 5) indicate that there are substantial discrepancies in depicting the strength of the major $E - P$ zones. For instance, the $E - P$ minimum at ~8°N in the tropical wet zone differs by up to 130 cm yr^{-1}. NCEP1 and 20CR have the weakest net P of −70 cm yr^{-1}, while ERA-40 and JRA-55 have the strongest net P, exceeding −200 cm yr^{-1}. Unlike JRA-55, where the strong net P in the tropics is accompanied by a strong net E in the subtropics, MERRA-2 shows a relatively weaker net P in the tropics but a very high net E in the subtropics, and the large $E - P$ budget in MERRA-2 (Fig. 3a) is related to excessive evaporation in the subtropical dry zones.

Differences between GPCP and CMAP are also found. The two P products have almost the same budget over the global ocean (Table 2), but CMAP is weak at the subpolar latitudes. The combined OAFlux-CMAP,

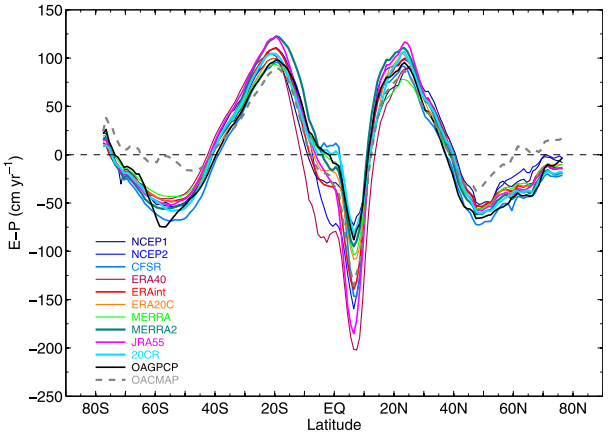

FIG. 5. Zonal mean average of $E - P$.

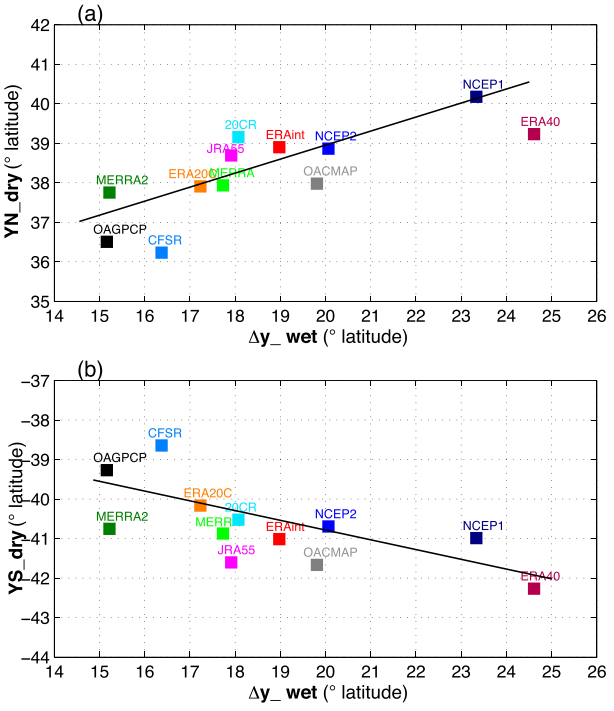

FIG. 6. The width of the tropical wet zone (x axis) vs the latitudinal position of the poleward edge of the subtropical dry zone (y axis) in the (a) Northern Hemisphere and (b) Southern Hemisphere.

which is considerably dry at higher latitudes, is distinctly different from the group. Yin et al. (2004) pointed out that while the use of atoll gauge data may be a source of the tropical bias in CMAP, the cold-season P is an uncertainty source for all products at high latitudes.

One subtle but nonetheless noteworthy difference between products is the latitudinal position of the tropical and subtropical zones. Compared to OAFlux-GPCP, the reanalyses have a broader tropical wet zone, which consequently pushes the north and south subtropical dry zones poleward. To provide a more quantitative perspective, the latitudinal positions of zero $E - P$ were derived from the zonal mean averages and the following indices were constructed: the width of the tropical wet zone (denoted as Δy_wet), the northern edge of the northern subtropical dry zone (denoted as YN_dry), and the southern edge of the southern subtropical dry zone (denoted as YS_dry). The relationship of Δy_wet (the x axis) with the respective YN_dry and YS_dry (the y axis in Figs. 6a,b) indicate that, compared to OAFlux-GPCP, YN_dry and YS_dry are poleward displaced, by as much as 1°–3° of latitude, in all reanalyses except for CFSR. The spread in Δy_wet among products is significant, from 15°–16° of latitude (OAFlux-GPCP, MERRA-2, and CFSR) to nearly 25° of latitude (NCEP1 and ERA-40). ERA-40 and NCEP1 have the most extensive tropical wet zone and the farthest displaced subtropical dry zones.

The consistency among MERRA-2, CFSR, and OAFlux-GPCP in depicting Δy_wet is interesting. The two reanalyses correct the model-generated P over land by using the CMAP/GPCP/CPCU observation-based merged products (Saha et al. 2010; Bosilovich et al. 2015). The correction seems to be effective in constraining the Δy_wet to be ~15° of latitude in the model. Another possibility is the use of a similar convective parameterization and a common Gridpoint Statistical Interpolation (GSI) analysis scheme in both reanalyses which might have as much or more effect on the wet/dry zone structure. The remaining seven products show a Δy_wet that is 3°–8° latitude broader. One surprising difference is found between the two satellite-based P products: CMAP leads to a Δy_wet that is 5° latitude broader than GPCP. As the two products were constructed from similar satellite observations (Yin et al. 2004), it is not clear what contributed to the differences in the meridional extent of the tropical rainband.

e. *Relationship between the* E − P *strength and the zone width*

To explore whether the width of the tropical wet zone is a main contributor to the uncertainty of $E - P$ in each zone, the relationship between zone-averaged $E - P$ and the zone width in the 12 products was constructed for the three zones: the subtropical dry zones of both northern and southern hemispheres and the tropical wet zone (Figs. 7a–c). Except for a few outliners, there is a loose linear relationship in all zones, implying that the $E - P$ budget increases with the zone width. For instance, the broader MERRA-2, JRA-55, and NCEP2 correspond with a higher $E - P$ budget in the subtropics. In the tropical wet zone, JRA-55 and NCEP2 are on the higher

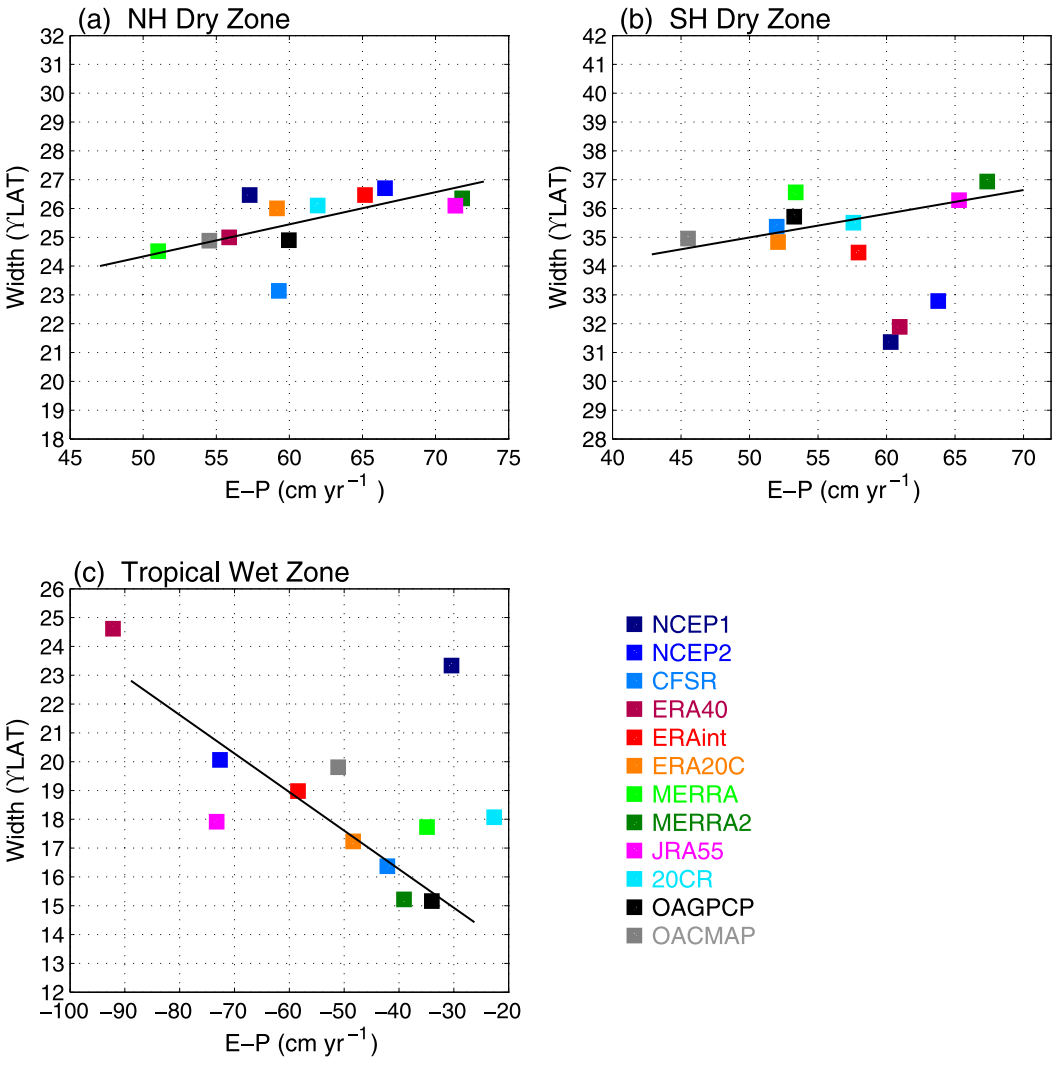

FIG. 7. The $E - P$ budget vs the meridional extent of the zone. (a) The subtropical dry zone in the Northern Hemisphere, (b) the subtropical dry zone in the Southern Hemisphere, and (c) the tropical wet zone.

end of the chart (if the erroneous ERA-40 is not considered), and MERRA-2 falls to the lower end at a level similar to OAFlux-GPCP. The budget imbalance between the tropical and subtropical zones is the source of the large $E - P$ imbalance over the global scale (Fig. 3a).

In general, the relationship between the $E - P$ budget and zone width has more scatter in the tropical than in the subtropical zones. The strength and width of the tropical precipitation associated with the ITCZ/SPCZ depend on internal dynamic and thermodynamic processes and their complex feedback interaction with SST (Schneider et al. 2014). No simple relationship should be expected between the width and strength of the ITCZ/SPCZ. The spread in the tropical $E - P$ budget is as large as its mean $E - P$, indicating that there is a high degree of uncertainty in $E - P$ estimates.

The spread in time-mean spatial distribution of the zero $E - P$ locations between the 12 products was constructed (Fig. 8). All products agree well on the meridional extent of the ITCZ rainfall in the eastern tropical Pacific, but they deviate from each other in the western tropical Pacific, the SPCZ, and the western Indian Ocean/Arabian Sea. The pattern of differences suggests the uncertainty of reanalyses in simulating tropical convective clouds and rainfall processes over the Indo-Pacific warm pool (Rosenfeld and Lensky 1998; Newman et al. 2000).

f. Seasonal variability of $E - P$ and its uncertainty in the wet/dry zones

The wet/dry zones wax and wane seasonally, in response to the seasonal movement of the ITCZ and the subtropical high pressure cells. The seasonal change of

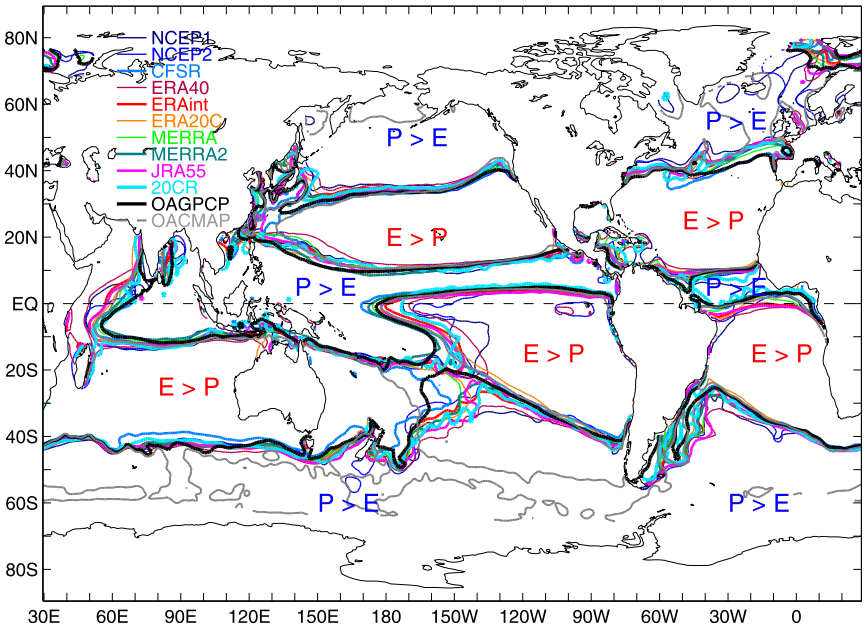

FIG. 8. Spatial distribution of the $E - P$ zero lines.

the wet/dry zones and the uncertainty of $E - P$ within the zones were depicted using the zonally averaged climatological monthly-mean $E - P$ field (Figs. 9a,b). In addition, the zero $E - P$ lines derived from all products were superimposed to delineate the degree of inconsistency between products. The strengthening and expansion of the northern and southern subtropical dry zones occur during the winter season of the respective hemisphere. The tropical wet zone is narrowest and strongest during June–August when the ITCZ is at the northernmost location. The products have a better agreement in positioning the fringe of the northern subtropical dry zone than the southern counterpart, but they disagree largely on the position of the near-equatorial edge of the southern subtropical dry zone during the austral winter. The STD of the $E - P$ differences between products (Fig. 9b) shows that the major source of uncertainty on seasonal time scales resides in the tropical wet zone.

The subtropical dry zone is at maximal meridional extent during the winter of the respective hemisphere (Figs. 10a,b). Reanalyses tend to be comparable to one another in depicting the seasonal change of the northern dry zone, but differ among themselves in producing the change of the southern dry zone. The problem in the latter reflects primarily the uncertainty in the position of the near-equatorial edge of the southern dry zone during June–November (Figs. 10a,b). For the tropical zone (Fig. 10c), most products have two seasonal contractions, one in June and the other in November, and two seasonal expansions, one in August and the other in December. We speculate that the disparity in the products may be related to the problems of reanalyses to represent the global monsoon and particularly the Northern Hemisphere (NH) Asian monsoon (Wang and Ding 2008). It is observed (Fig. 9) that uncertainty in products is low during the NH winter when large-scale dynamics are in control, and the uncertainty increases during the NH monsoon onset time when skill or consensus in reanalysis models breaks down.

The zone's area changes with products. To have a fair comparison, we computed the monthly evolution of the zone-averaged $E - P$ budget using the zero $E - P$ positions derived from the respective products. The 12 products achieve the best consistency in depicting the seasonal variations of the zone-averaged $E - P$ in the northern subtropical dry zone (Fig. 11a), featuring a seasonal low ($\sim$20–40 cm yr^{-1}) in August and a seasonal high ($\sim$100–120 cm yr^{-1}) in December. The products, however, differ in the magnitude of $E - P$ by as much as 20 cm yr^{-1}, most evident during January–April. There is also a general agreement in seasonal $E - P$ changes in the southern subtropical zone (Fig. 11b), with a seasonal high (low) in June–August (November–January), although there are differences in the seasonal peak months. Some products, like ERA-Interim, NCEP1, and ERA-40, produce a sharp seasonal peak in June or July while the others have a broad peak of 3–4 months, from June to August. The spread in the magnitude of the zone-averaged $E - P$ exceeds 20 cm yr^{-1} throughout the year, largest during May–August.

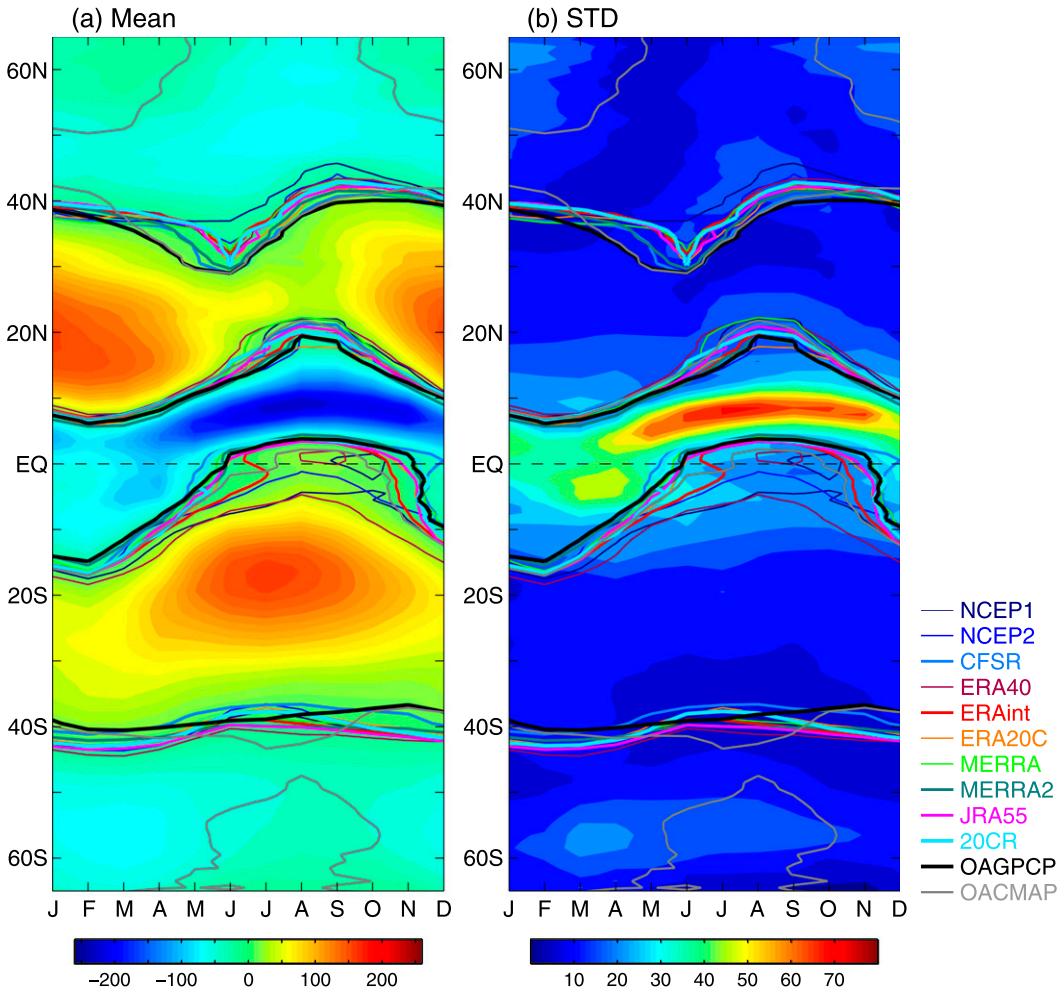

FIG. 9. Seasonal variations of zonally averaged (a) ensemble $E - P$, and (b) STD of the spread in $E - P$. The $E - P$ zero lines for the 12 products are superimposed. The unit is cm yr^{-1}.

The products have the least consistency in the tropical wet zone, where the spread in the magnitude amounts more than 100 cm yr^{-1} and the differences in the seasonal cycle are so large that no two products are alike (Fig. 11c). The two satellite P products, CMAP and GPCP, have a better agreement in pattern of seasonal change but not in magnitude. CMAP has a stronger P, not only in the tropical zone but also in the subtropics. Compared to OAFlux-GPCP, OAFlux-CMAP tends to have a weaker $E - P$ gain in the dry zones and a stronger $E - P$ deficit in the tropical region. OAFlux-GPCP is more in line with most reanalyses in terms of the pattern of the seasonal cycle. Other studies (Schanze et al. 2010; Ren et al. 2014) have also suggested that OAFlux-GPCP has a better consistency with ocean salinity observations than OAFlux-CMAP.

There is an asymmetry in the uncertainty level of the $E - P$ estimates between the wet and dry zones, and the bias is highly regime dependent. The $E - P$ estimates in the tropical wet zone are more problematic. Presumably, the wet zone, featuring the complex ITCZ/SPCZ/warm pool physics, poses a higher degree of challenges on models than the dry zone. No model is capable of simulating the multiplex array of processes and scales that occur in tropical convection and storms, including wind patterns, cloud particles, and rain from the heavily raining updraft regions (so-called convective areas) to less violent and lighter-raining broad regions (so-called stratiform areas). The inability is in part because of the lack of understanding of many key processes and in part because of the difficulty in parameterizing the complexity associated with subgrid processes in large-scale atmospheric models (e.g., Newman et al. 2000; Trenberth et al. 2001).

g. *Can salinity be used to assess the uncertainty of* E − P*?*

To the first order, the time-mean features of the freshwater cycle are reflected in the time-mean surface salinity field (Fig. 12a), with low SSS associated with the

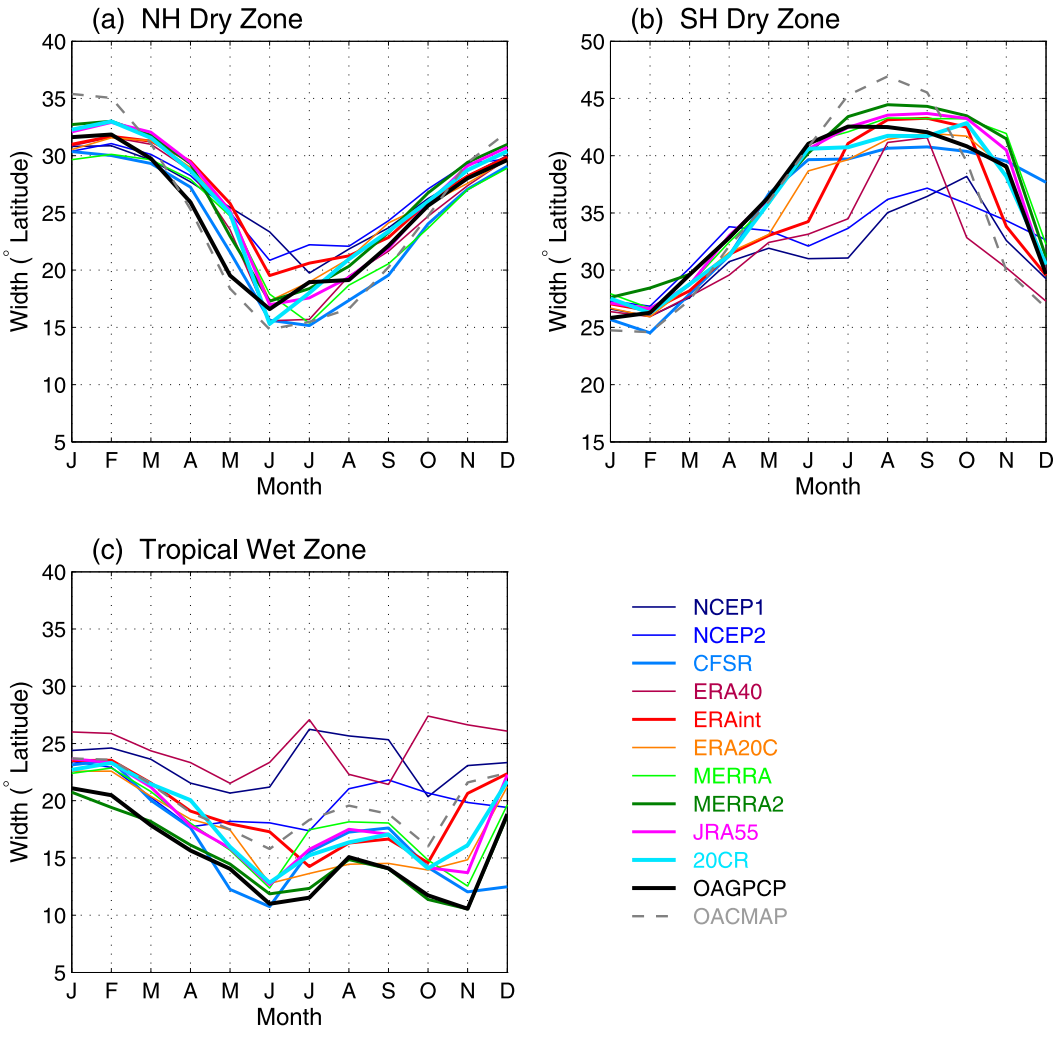

FIG. 10. Seasonal variations of the meridional extent of (a) the subtropical dry zone in the Northern Hemisphere, (b) the subtropical dry zone in the Southern Hemisphere, and (c) the tropical wet zone.

tropical wet zone and high SSS with the subtropical dry zones. Nevertheless, the $E - P$ maxima/minima and the salinity maxima/minima do not exactly collocate (Fig. 12b), as the $E - P$ peaks are more equatorward. The largest seasonal variances of SSS are located a few degrees more equatorward than the largest ITCZ-related $E - P$ variability (Fig. 12c). The mismatches between $E - P$ and the surface salinity are an indication that the change of ocean salinity is driven not only by the surface $E - P$ flux but also by upper ocean dynamical processes (Yu 2011). For the two SSS products in use, *Aquarius* SSS has a larger seasonal STD than Argo mixed layer salinity (MLS), particularly in the tropical wet regions. The differences may be related to the better spatial resolution provided by satellite sensor and/or the depth difference satellite salinity that represents the salinity at the top cm of the ocean and Argo salinity that is measured at 5 m below the surface.

SSS may be used as an indicator of $E - P$ forcing in regions where the effects of ocean dynamics are less dominant. To determine such regions, we start by examining the following mixed-layer salinity budget equation (Mignot and Frankignoul 2003; Yu 2011):

$$\underset{\text{(I)}}{\frac{\partial S'}{\partial t}} \approx \underset{\text{(II)}}{\frac{\overline{S}(E' - P')}{\overline{h}}} - \underset{\text{(III)}}{\overline{\mathbf{U}} \cdot \nabla S'} - \underset{\text{(IV)}}{\mathbf{U}' \cdot \nabla \overline{S}} - \underset{\text{(V)}}{\frac{[w_e \Gamma(w_e)(S - S_b)]'}{\overline{h}}} + \underset{\text{(VI)}}{\kappa \nabla^2 S'}, \quad (1)$$

where the overbar denotes the annual mean and the prime denotes the seasonal anomaly referenced to the

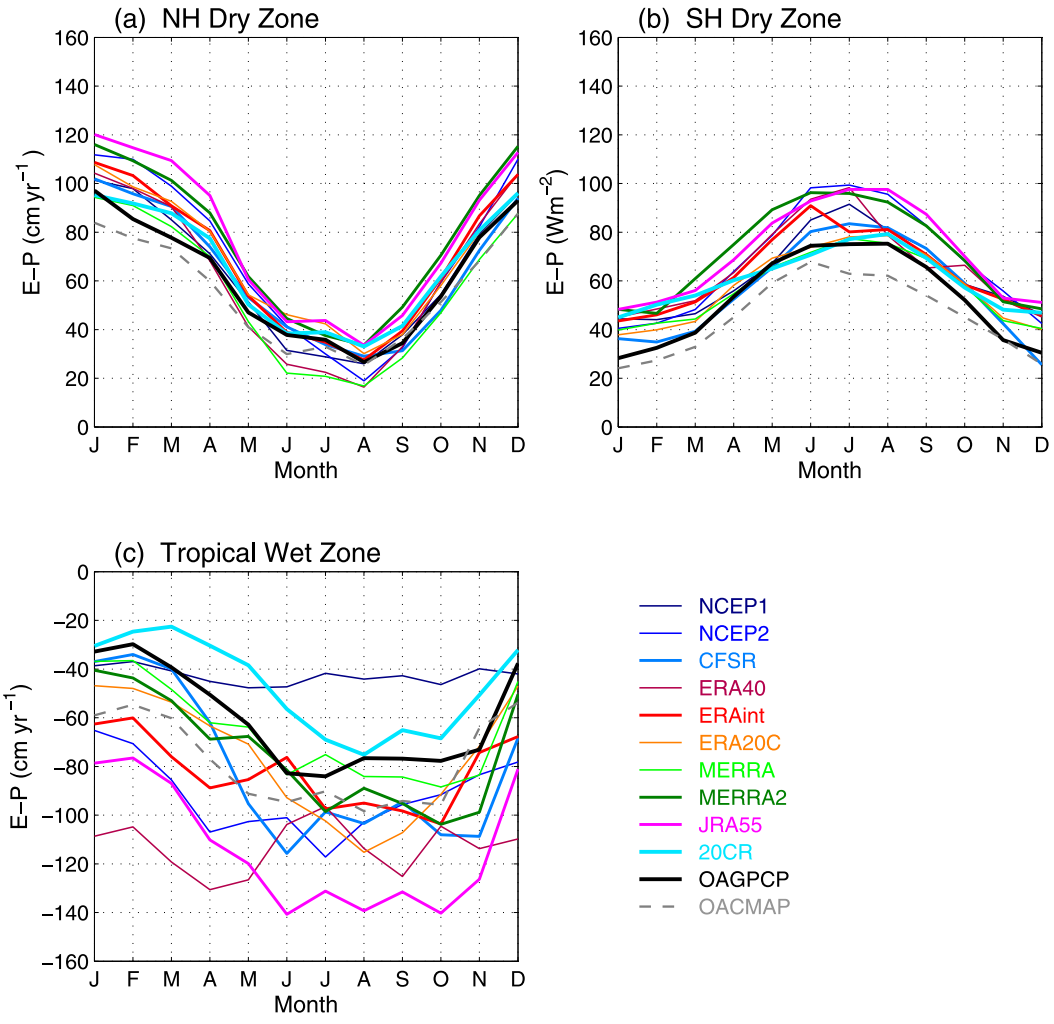

FIG. 11. Seasonal variations of the $E - P$ budget of (a) the subtropical dry zone in the Northern Hemisphere, (b) the subtropical dry zone in the Southern Hemisphere, and (c) the tropical wet zone.

mean; S is the salinity averaged vertically within the mixed layer with a depth of h, $\mathbf{U}$ is the horizontal velocity in the mixed layer, w_e is the entrainment velocity at depth $z = h$, S_b is the salinity right below h, and κ is the horizontal mixing coefficient and set to 500 m s^{-2}. Also, Γ is the Heaviside function, which is 1 if w_e is upward (entrainment) and 0 if w_e is downward (detrainment). The mixed layer depth is based on the potential density different criterion of 0.125 kg m^{-3}.

The entrainment velocity w_e in Eq. (1) is the vertical velocity relative to the moving mixed-layer base. It consists of vertical Ekman velocity w_{EK} and the h tendency (i.e., the vertical velocity of the mixed-layer base):

$$w_e = w_{\mathrm{EK}} + \left(\frac{\partial h}{\partial t} + \nabla \cdot h\mathbf{U}\right) = \frac{\nabla \times \boldsymbol{\tau}}{\rho f} + \left(\frac{\partial h}{\partial t} + \nabla \cdot h\mathbf{U}\right), \quad (2)$$

where $\boldsymbol{\tau}$ is the wind stress.

Yu (2011) computed the contribution of each term on the right-hand side in Eq. (1) to the change of salinity (the left-hand side) and obtained a global map that outlines the leading forcing for seasonal variability of surface salinity in different dynamic regimes using the salinity climatology of the *World Ocean Atlas* (*WOA*; Antonov et al. 2006). The map serves as a framework for this study as it provides a way to identify the $E - P$ influence regime. Here we updated the map using the salinity datasets from *Aquarius* and Argo along with the $E - P$ forcing and the ocean advection processes computed over the same 2012–14 period when *Aquarius* has a complete coverage of three full seasonal cycles. The maps on the percentage of salinity tendency variances that can be explained by $E - P$ are compared (Figs. 13a–c). There is a consistency among the three

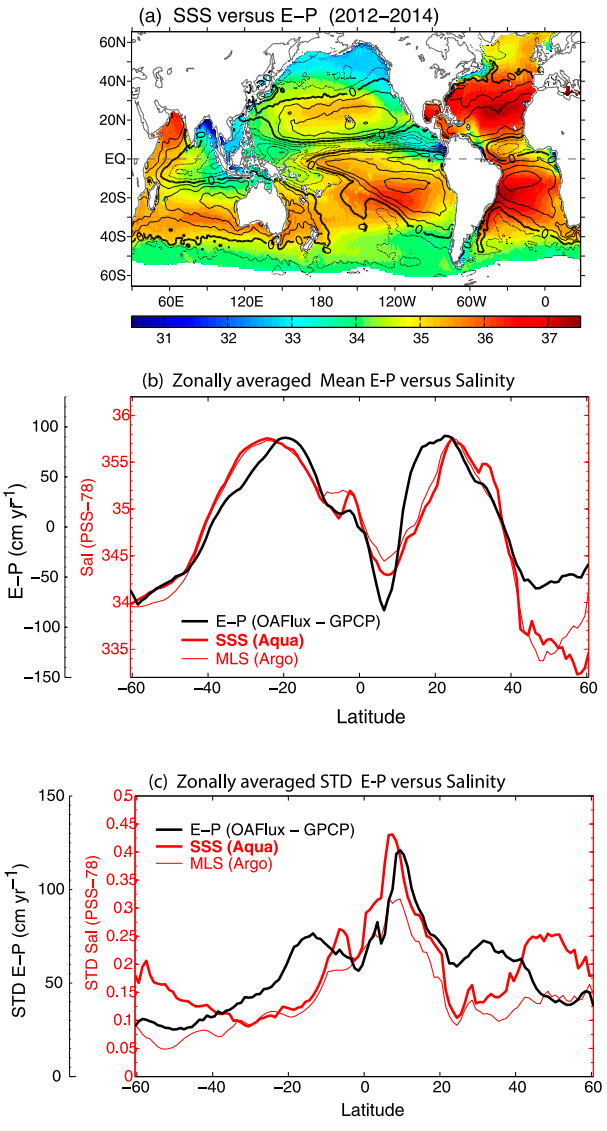

FIG. 12. (a) Mean *Aquarius* SSS with the $E - P$ contours (black) of the same three years superimposed. (b) Zonal mean average of *Aquarius* SSS (thick red), Argo MLS (thin red), and $E - P$ from OAFlux-GPCP (black). (c) Zonal average of seasonal STD of *Aquarius* SSS (thick red), Argo MLS (thin red), and $E - P$ from OAFlux-GPCP (black) All fields are based on the 3-yr climatology of 2012–14.

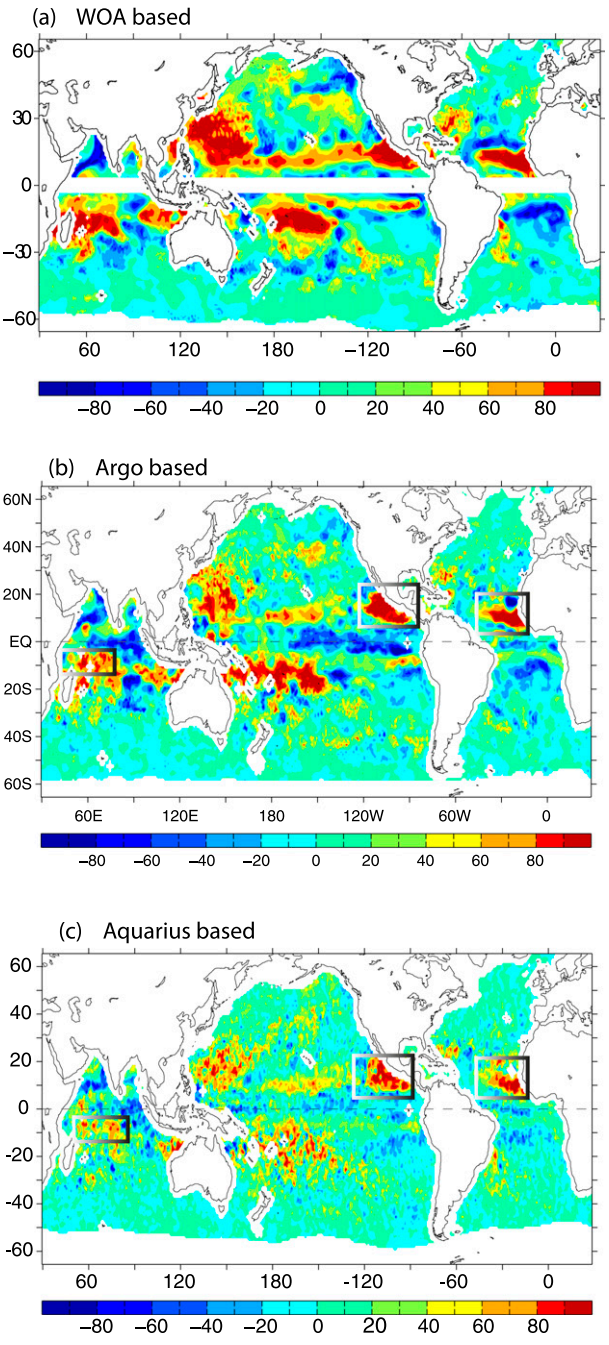

FIG. 13. The percentage of seasonal variances of surface salinity that can be explained by $E - P$ from OAFlux-GPCP based on (a) *WOA* MLS, (b), Argo MLS, and (c) *Aquarius* SSS. The three boxed areas are chosen as the test sites for using salinity to assess the uncertainty in $E - P$ products.

maps in depicting the dominance of the $E - P$ forcing along the tropical ITCZ/SPCZ. However, the percentage reduces considerably in the central tropical Pacific when Argo and *Aquarius* salinity data are used in place of *WOA* data. The sample resolution in the three salinity datasets differs. *Aquarius* is on 150 km every 7 days, Argo featuring nominal resolution on 3° × 3° every 10 days, and *WOA* on 1° constructed from a database with large spatial and temporal inhomogeneity. The reduced covariance indicates that the representation of the salinity advection (terms III and IV) improves with the higher-resolution salinity datasets because horizontal gradients of salinity are better produced.

Yu (2014, 2015) reported the existence of a shallow salinity minimum zone (SMZ) in the vicinity of the ITCZ/SPCZ, as a result of the oceanic Ekman convergence of the rain-freshened surface waters. Once formed, the SMZ is carried poleward away from the formation site by Ekman transport, which suggests that the transient nature of the low salinity distribution in the tropics is dominated primarily by the wind-driven Ekman dynamics. In Eq. (1), the effect of the Ekman dynamics on salinity spatial distribution is represented by terms III and IV. The magnitude of the two terms depends on the salinity spatial gradients and, hence, the spatial/temporal resolution in the dataset. *WOA* is overly smooth and produces weak spatial gradients (not shown), and hence the contribution of terms III and IV is weak. Consequently, the role of $E - P$ forcing is comparably boosted. Nonetheless, the percentage of the $E - P$ covariances with salinity tendency remains high (>60%) in three regions regardless of the differences in the effective spatial resolutions between the salinity datasets. These three regions include the eastern tropical Pacific east of 120°W, the eastern Atlantic east of 30°W, and the central southern Indian Ocean near 10°S. The robustness of the $E - P$ dominance on salinity variability in these three regions suggests that these sites could be used as a test bed for using salinity as a diagnosis tool for the $E - P$ uncertainty.

h. *Salinity-based evaluation of the tropical* E − P *variability*

The three boxed regions (Figs. 13a–c) are all located in the tropical wet zone. They are called the tropical eastern Pacific (EPAC) box, the tropical eastern Atlantic (EATL) box, and the southern Indian Ocean (SIO) box, respectively. For the three complete years (2012–14) covered by *Aquarius*, the available $E - P$ products include OAFlux-GPCP and OAFlux-CMAP and seven reanalyses (NCEP1, NCEP2, CFSR, ERA-Interim, MERRA, MERRA-2, and JRA-55). Argo salinity for the same period is also used to assist the diagnosis. In the following, we present the 3-yr composite seasonal time series of salinity tendency [term I of Eq. (1)] and the tendency due to $E - P$ forcing [term II of Eq. (1)] for each of the three regions (Figs. 14a–c). We show also the Taylor diagrams to summarize the correlation between $E - P$ forcing and salinity tendency, and the standard deviations of the two terms for each region (Figs. 14d–f).

At the EPAC site (Fig. 14a), the seasonal change of $E - P$ peaks during July–October, when the ITCZ is at the seasonal northernmost location. The amplitude of the seasonal cycle varies with products, with the JRA-55 and NCEP2 being strongest. While NCEP1 has a weak seasonal cycle with a very different seasonal phasing from the rest, all other products correlate well with the salinity tendency term (ΔS). The ΔS values for both *Aquarius* SSS and Argo MLS are shown, and the former has larger seasonal amplitude than the latter, likely due to the better sampling by *Aquarius* as well as the near-surface salinity stratification. Note that the seasonal cycle of ΔS plotted here is shifted forward by 1 month to improve the visual comparison between ΔS and $E - P$. A lagged response of ΔS to $E - P$ is also observed at the EATL and SIO sites, with a 2-month lag for the former and a 1-month lag for the latter. The 1–2-month longer lags at the three locations suggest that not all SSS tendency anomalies are explained by $E - P$ (Fig. 13). While $E - P$ contributes to 60%–80%, the ocean processes (and/or noise in the data) account for the remaining 20%–40% of variance.

At all three sites, JRA-55 has the strongest seasonal cycle followed by NCEP2. In addition, CFSR has a large peak in August at the EATL site, while ERA-Interim displays a similar strong intensity as JRA-55 at the SIO site. The Taylor diagrams (Figs. 14d–f) are made in polar coordinates, where the angle represents correlation r that is given by $\theta = \cos^{-1} r$, and the radius R is the STD of the $E - P$ anomalies. The root-mean-square (rms) error of each time series is the distance of the each time series (colored dot) to *Aquarius* ΔS (orange dot) on the x axis. At the EPAC site, all the $E - P$ time series have a correlation equal to or greater than 0.8, except for NCEP1, which shows a very low correlation of 0.1. All have a STD magnitude that is equivalent to STD ΔS, except for NCEP1 (too low) and JRA-55/NCEP2 (too high). NCEP1, NCEP2, and JRA-55 have also a larger rms error than other products. At the EATL site, the correlation of the $E - P$ products with *Aquarius* ΔS is considerably lower, with all of them being less than 0.6. The rms error is higher, with JRA-55 again being largest. JRA-55 also shows a large seasonal STD, while the other products have an overall similar STD magnitude comparable to *Aquarius* ΔS. At the SIO site, JRA-55, NCEP2, and ERA-Interim seem to be less comparable to *Aquarius* ΔS than other products.

Because of the role of ocean dynamics, our ability to assess which $E - P$ product is more accurate in describing the seasonal variability in these regions is subject to threshold level of 20%–40% (Fig. 13). Nonetheless, the spread of the $E - P$ products is larger than the observational uncertainty. For example, at the EPAC and EATL sites, the range of the $E - P$ forcing tendency is 0.5–0.6 pss per month in August. Even if

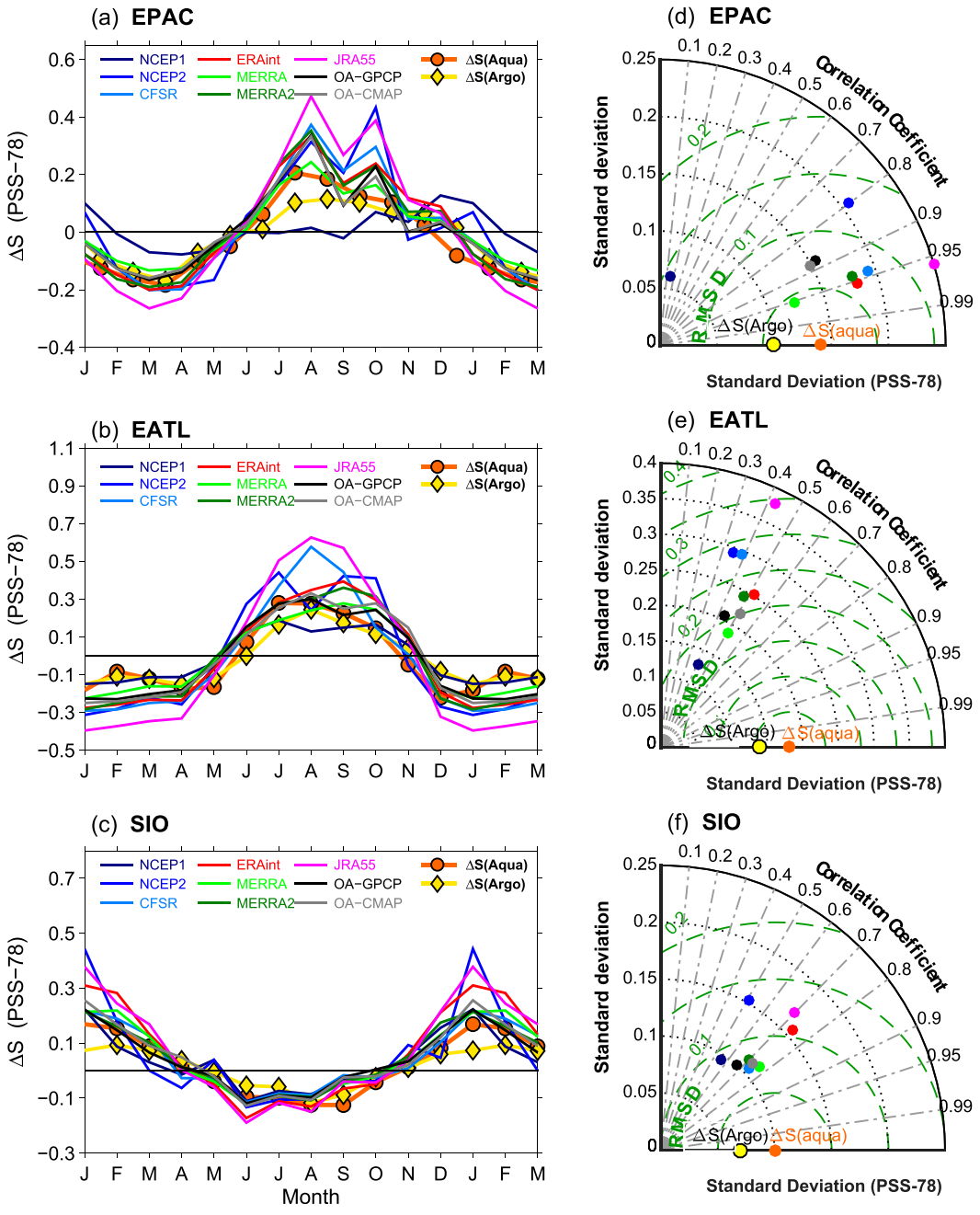

FIG. 14. Salinity-based evaluation of the $E - P$ products forced seasonal variation of SSS tendency for the three boxed areas: (a) EPAC, (b) EATL, and (c) SIO. The orange and yellow curves denote the seasonal SSS tendency anomalies estimated from *Aquarius* and Argo data. The curves with other colors represent the inferred changes of SSS tendency forced by seasonal $E - P$ products. Summary of the comparison statistics are presented by the Taylor diagram for (d) EPAC, (e) EATL, and (f) SIO, where the angle represents correlation r that is given by $\theta = \cos^{-1} r$, and the radius R is the STD of the anomalies. The root-mean-square (rms) error of each product is the distance of the product (colored dot) to *Aquarius* ΔS (the orange dot) on the x axis. The STD of Argo salinity is added to the x axis (yellow dot) as a reference.

excluding NCEP1, the remaining range of spread is about 0.3–0.4 pss per month. The accuracy of *Aquarius* V4 CAP data product in the tropics is less than 0.2 pss on monthly time scale at 150-km spatial scale (Tang et al. 2014). The spatial average within the box would further reduce the data uncertainty, as the difference between *Aquarius* and Argo ΔS is less than 0.1 pss. Lee (2016; Fig. 3) also showed that the accuracy of *Aquarius* V4

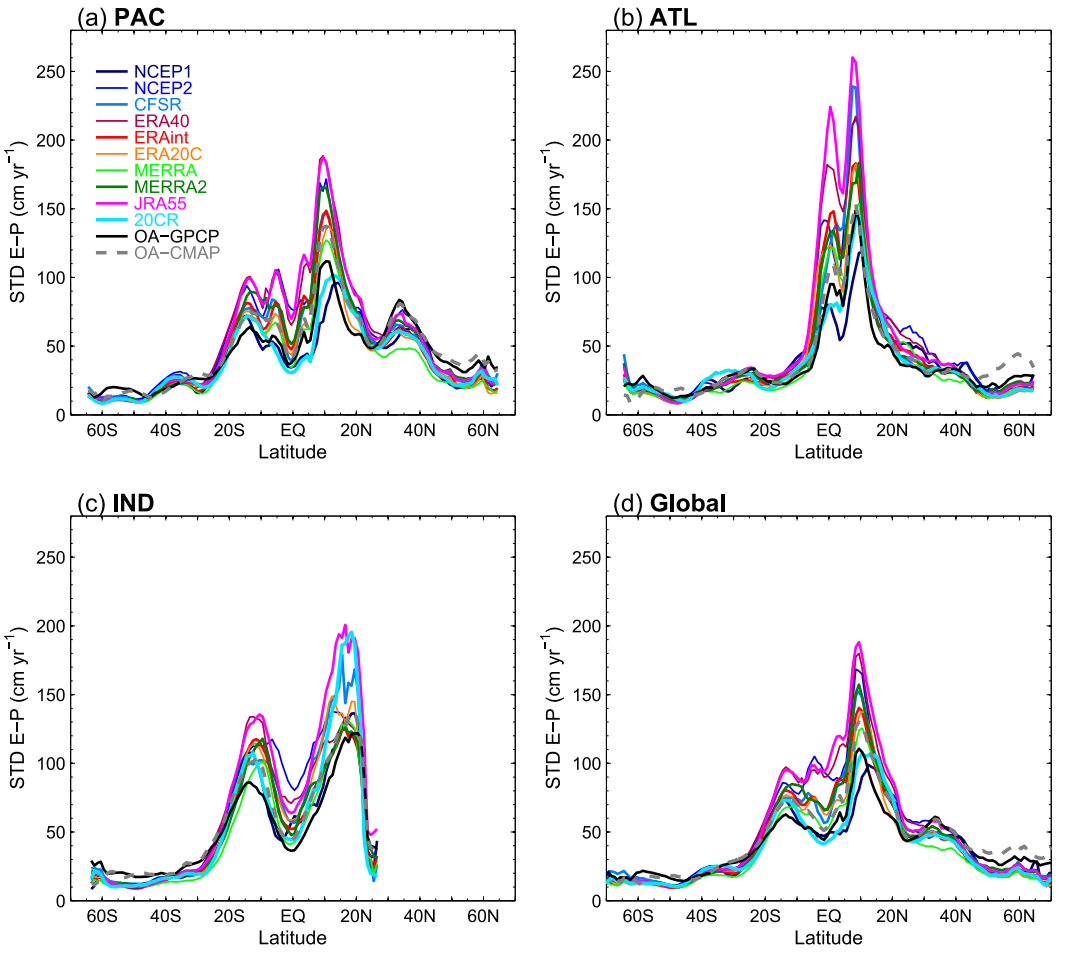

FIG. 15. Zonal average of seasonal STD in the (a) Pacific, (b) Atlantic, (c) Indian, and (d) global oceans.

product should be in a range of 0.05–0.1 pss for the three regions discussed here.

i. Seasonal variability of E − P *and its spread over the global basins*

The salinity evaluation (Fig. 14) indicates that seasonal variability of the tropical $E - P$ from JRA-55 and NCEP2 is largely overestimated during the 3-yr *Aquarius* observing period. Since the tropical $E - P$ dictates the global uncertainty structure of the seasonal cycle in $E - P$ (Fig. 11), the regional indicator has an important global character. To show this, the seasonal STD of the global $E - P$ was computed and the zonal averages are shown for both global and regional basins for the Pacific, Atlantic, and Indian Oceans (Figs. 15a–d). The products display a similar latitudinal distribution of the seasonal STD in all basins, with the largest variability occurring in the tropical and subtropical latitudes. Among all 12 products, JRA-55, ERA-40, and NCEP2 have strong seasonal variability that is most prominent between 20°S and 20°N. This is consistent with the regional salinity evaluation, suggesting that the three products have an overestimated seasonal cycle.

The magnitude of seasonal STD in $E - P$ is driven predominately by the magnitude of seasonal STD in P, not in E. To illustrate this more clearly, the seasonal STD fields of $E - P$, E, and P were averaged globally and the relationship between STD $E - P$ (y axis) with the respective STD E and STD P (x axis) is constructed for all products (Figs. 16a,b). The products have a relatively small spread in STD E, ranging from 20 cm yr^{-1} (MERRA) to 31 cm yr^{-1} (NCEP2), but a large spread in STD $E - P$, from ~44 cm yr^{-1} (MERRA, OAFlux-GPCP, NCEP1, and 20CR) to ~62 cm yr^{-1} (JRA-55, NCEP2, and ERA-40) (Fig. 16a). The large spread in STD $E - P$ is dominated by the large spread in STD P (Fig. 16b), as the latter ranges from 40 cm yr^{-1} (OAFlux-GPCP, MERRA, NCEP1, and 20CR) to 57 cm yr^{-1} (JRA-55, NCEP2, and ERA-40). The spread in P, particularly associated with the tropical ITCZ/SPCZ,

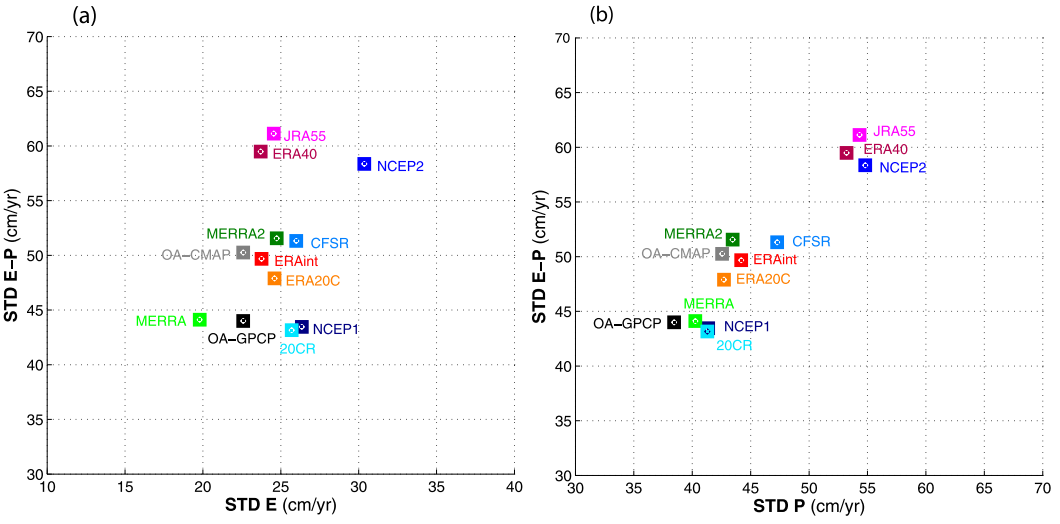

FIG. 16. The ratio of global ocean averaged (a) STD E to STD $E - P$, and (b) STD P to STD $E - P$.

determines the structure and magnitude of the uncertainty in the seasonal cycle of $E - P$.

4. Summary and concluding remarks

This study provided an assessment of the freshwater cycle over the global open ocean using the $E - P$ products from10 reanalyses (including NCEP1, NCEP2, ERA-40, CFSR, ERA-interim, JRA-55, MERRA, MERRA-2, ERA-20C, and 20CR), two combined satellite-based $E - P$ analyses (OAFlux-GPCP and OAFlux-CMAP) (Table 1), and two salinity observation products. Three issues are examined: 1) the uncertainty level in the ocean-surface freshwater budget in the present atmospheric reanalyses, 2) the uncertainty structure and association with the global ocean wet/dry zones, and 3) the potential of *Aquarius* satellite salinity in ascribing the uncertainty in $E - P$. The main results are summarized as follows. Note that ERA-40 is not included in the following discussion as its $E - P$ budget is erroneous (Table 2).

1) Ocean-surface freshwater budgets: The products agree on the large-scale time-mean pattern of $E - P$, but differ considerably in magnitude (Figs. 1–3). The OS freshwater budgets based on the ensemble of the products are 129 ± 10 (8%) cm yr^{-1} for E, 118 ± 11 (9%) cm yr^{-1} for P, and 11 ± 4 (36%) cm yr^{-1} for $E - P$ (Table 2), where the error bars are the standard deviations of the spread between products. The $E - P$ uncertainty exceeds the uncertainty in E and P by a factor of 4 or more.
2) Uncertainty in the width and strength of the wet/dry zones: The large uncertainty in $E - P$ is attributed to P in the tropical wet zone (Figs. 1 and 5). Most reanalyses tend to produce a wider tropical rainband when compared to satellite products (Figs. 6 and 7), with the exception of two recent reanalyses that implement an observation-based correction for the model-generated P over land. The disparity in the width and the extent of seasonal variations of the tropical wet zone causes large spread in P, implying that the tropical moist physics and the realism of tropical rainfall remain a key challenge.
3) Uncertainty in seasonal variations of the $E - P$ budget: Reanalyses have a broad agreement on seasonal variations of the $E - P$ budget in the northern and subtropical dry zones (Figs. 10 and 11) but deviate greatly in depicting the seasonal movement of the southern edge of the tropical wet zone, particularly during June – November. The disparity in the products may be related to the problems of reanalyses to represent the global monsoons and particularly the NH Asian monsoon. The low uncertainty during the NH winter is when large-scale dynamics are in control, and high uncertainty at NH monsoon onset times is when skill or consensus in reanalysis models breaks down.
4) Ocean salinity as a rain gauge for evaluating the $E - P$ products: Three boxed regions, all located in the tropical wet zone, are identified as potential areas for evaluating the uncertainties in the $E - P$ products (Fig. 13). At these sites, the salinity evaluation indicates that $E - P$ seasonal variances from JRA-55 and NCEP2 are largely overestimated whereas those from NCEP1 are underestimated. The regional diagnosis is consistent with the uncertainty level of the global $E - P$ in these products, suggesting the global

indication of the tropical evaluation. The spread among $E - P$ products in terms of implied seasonal salinity tendency exceeds the salinity observation uncertainty (including the difference between *Aquarius* and Argo), which gives the confidence on the use of ocean salinity observations as verification dataset.

5) Concluding remarks: A key finding of the study is that the ocean-surface $E - P$ budget in atmospheric reanalyses that are presently available has large uncertainty, and the magnitude of uncertainty exceeds that in E and P by a factor of 4 or more. The uncertainty is attributed primarily to the P estimates in the tropical wet zone, and secondarily to E estimates. The asymmetric bias structure reflects the greater degree of difficulties in modeling the physical processes associated with P, particularly, in the ITCZ/SPCZ region where the width and the extent of seasonal migration of the tropical wet zone vary considerably with product. Our study is consistent with existing literature in that the moist physics and the realism of tropical rainfall remain a key challenge for atmospheric reanalysis. We found that CFSR and MERRA-2 appear to do well in simulating the width and strength of the tropical wet zone compared to satellite-based products, perhaps benefitting from the correction of the model-generated precipitation over land using P observation products. Nevertheless, the $E - P$ budget in the two reanalyses is out of balance in the subtropical dry zones, leading to the global $E - P$ budget to be smallest in CFSR ($4\,\mathrm{cm\,yr^{-1}}$) and largest in MERRA-2 ($21\,\mathrm{cm\,yr^{-1}}$). The freshwater budget over the ocean is sensitive to the constraints of the moisture budget implemented in the reanalysis. Satellite salinity appears feasible to evaluate the fidelity of $E - P$ variability in three tropical areas, where the uncertainty diagnosis has a global indication. However, the limited regimes where the majority of the $E - P$ variance can be explained by salinity measurements limit the value of salinity in leading to atmospheric reanalysis improvements. Perhaps salinity measurements will find a greater contribution in the context of coupled reanalyses, which will soon become a standard methodology.

Acknowledgments. Primary support for the study is provided by the NOAA Modeling, Analysis, Predictions, and Projections (MAPP) Program's Climate Reanalysis Task Force (CRTF) through Grant NA13OAR4310106. Mike Bosilovich is sincerely thanked for his input on MERRA-2. The lead author (L. Yu) acknowledges the support of NOAA Climate Observation Division (COD) Grant NA09OAR4320129 for the OAFlux evaporation dataset and NASA Ocean Surface Salinity Science Team (OSSST) Grant NNX12AG93G for the project on satellite salinity and the ocean water cycle. The research by T. Lee was carried out at the Jet Propulsion Laboratory, California Institute of Technology, under a NASA contract. ERA-40, ERA-Interim, and JRA-55 were downloaded from the NCAR Research Data Archive at http://rda.ucar.edu. CFSR was from the NOAA National Operational Model Archive and Distribution System (NOMADS) at ftp://nomads.ncdc.noaa.gov/CFSR/ (1979–2009) and from the NCAR Research Data Archive at http://rda.ucar.edu (after 2009). NCEP1, NCEP2, 20CR (v2c), and CMAP were from NOAA Earth System Research Laboratory (ESRL) Physical Sciences Division (PSD) at http://www.esrl.noaa.gov/psd/. MERRA and MERRA-2 were from the NASA Goddard Earth Sciences (GES) Data and Information Services Center (DISC) at http://disc.sci.gsfc.nasa.gov. ERA-20C was from ECMWF at http://www.ecmwf.int/en/research/climate-reanalysis/era-20c. GPCP monthly precipitation analysis was from http://eagle1.umd.edu/GPCP_CDR/Monthly_Data/. OAFlux evaporation was from http://oaflux.whoi.edu/. *Aquarius* salinity data were from ftp://podaac-ftp.jpl.nasa.gov/allData/aquarius/L2/CAPv4. Argo data (http://doi.org/10.17882/42182) were from http://www.argo.ucsd.edu/.

REFERENCES

Adler, R. F., and Coauthors, 2003: The version 2 Global Precipitation Climatology Project (GPCP) Monthly Precipitation Analysis (1979–present). *J. Hydrometeor.*, **4**, 1147–1167, doi:10.1175/1525-7541(2003)004<1147:TVGPCP>2.0.CO;2.

Antonov, J. I., R. A. Locarnini, T. P. Boyer, A. V. Mishonov, and H. E. Garcia, 2006: *Salinity*. Vol. 2, *World Ocean Atlas 2005*, S. Levitus, Ed., NOAA Atlas NESDIS 62, 182 pp.

Baumgartner, A., and E. Reichel, 1975: *The World Water Balance: Mean Annual Global, Continental and Maritime Precipitation and Run-Off*. Elsevier, 179 pp.

Bengtsson, L., S. Hagemann, and K. I. Hodges, 2004: Can climate trends be calculated from reanalysis data? *J. Geophys. Res.*, **109**, D11111, doi:10.1029/2004JD004536.

Bosilovich, M. G., J. Chen, F. R. Robertson, and R. F. Adler, 2008: Evaluation of global precipitation in reanalyses. *J. Appl. Meteor. Climatol.*, **47**, 2279–2299, doi:10.1175/2008JAMC1921.1.

——, F. R. Robertson, and J. Chen, 2011: Global energy and water budgets in MERRA. *J. Climate*, **24**, 5721–5739, doi:10.1175/2011JCLI4175.1.

——, and Coauthors, 2015: MERRA-2: Initial evaluation of the climate. Tech. Rep. Series on Global Modeling and Data Assimilation, Vol. 43, R. D. Koster, Ed., Goddard Space Flight Center, 139 pp.

——, F. R. Robertson, L. Takacs, A. Molod, and D. Mocko, 2016: Atmospheric water balance and variability in the MERRA-2 reanalysis. *J. Climate*, **30**, 1177–1196, doi:10.1175/JCLI-D-16-0338.1.

Chen, M., and P. Xie, 2008: CPC unified gauge-based analysis of global daily precipitation. *Proc. Western Pacific Geophysics*

Meeting, Cairns, Queensland, Australia, Amer. Geophys. Union. [Available online at ftp://ftp.cpc.ncep.noaa.gov/precip/CPC_UNI_PRCP/GAUGE_CONUS/DOCU/Chen_et_al_2008_Daily_Gauge_Anal.pdf.]

Compo, G., and Coauthors, 2011: The Twentieth Century Reanalysis Project. *Quart. J. Roy. Meteor. Soc.*, **137**, 1–28, doi:10.1002/qj.776.

——, J. Carton, X. Dong, A. Kumar, S. Saha, J. S. Woollen, L. Yu, and H. M. Archambault, 2016: Report from the NOAA Climate Reanalysis Task Force Technical Workshop. NOAA Tech. Rep. OAR CPO-4, 23 pp., doi:10.7289/V53J39ZZ.

Dai, A., T. Qian, K. E. Trenberth, and J. D. Milliman, 2009: Changes in continental freshwater discharge from 1948 to 2004. *J. Climate*, **22**, 2773–2792, doi:10.1175/2008JCLI2592.1.

de Boyer Montégut, C., G. Madec, A. S. Fischer, A. Lazar, and D. Iudicone, 2004: Mixed layer depth over the global ocean: An examination of profile data and a profile-based climatology. *J. Geophys. Res.*, **109**, C12003, doi:10.1029/2004JC002378.

Dee, D. P., and Coauthors, 2011: The ERA-Interim reanalysis: Configuration and performance of the data assimilation system. *Quart. J. Roy. Meteor. Soc.*, **137**, 553–597, doi:10.1002/qj.828.

Dickson, R. R., J. Meincke, S. A. Malmberg, and A. J. Lee, 1988: The "Great Salinity Anomaly" in the northern North Atlantic, 1968–1982. *Prog. Oceanogr.*, **20**, 103–151, doi:10.1016/0079-6611(88)90049-3.

Elliott, G. W., 1974: Precipitation signatures in sea-surface-layer conditions during BOMEX. *J. Phys. Oceanogr.*, **4**, 498–501, doi:10.1175/1520-0485(1974)004<0498:PSISSL>2.0.CO;2.

Fairall, C. W., E. F. Bradley, J. E. Hare, A. A. Grachev, and J. B. Edson, 2003: Bulk parameterization of air–sea fluxes: Updates and verification for the COARE algorithm. *J. Climate*, **16**, 571–591, doi:10.1175/1520-0442(2003)016<0571:BPOASF>2.0.CO;2.

Giglio, D., and D. Roemmich, 2014: Climatological monthly heat and freshwater flux estimates on a global scale from Argo. *J. Geophys. Res. Oceans*, **119**, 6884–6899, doi:10.1002/2014JC010083.

Gimeno, L., and Coauthors, 2012: Oceanic and terrestrial sources of continental precipitation. *Rev. Geophys.*, **50**, RG4003, doi:10.1029/2012RG000389.

Hagemann, S., K. Arpe, and L. Bengtsson, 2005: Validation of the hydrological cycle of ERA-40. ERA-40 Project Rep. Series, No. 24, ECMWF, 42 pp. [Available online at http://www.ecmwf.int/en/elibrary/9728-validation-hydrological-cycle-era-40.]

Hegerl, G. C., and Coauthors, 2015: Challenges in quantifying changes in the global water cycle. *Bull. Amer. Meteor. Soc.*, **96**, 1097–1115, doi:10.1175/BAMS-D-13-00212.1.

Hersbach, H., C. Peubey, A. Simmons, P. Berrisford, P. Poli, and D. Dee, 2015: ERA-20CM: A twentieth-century atmospheric model ensemble. *Quart. J. Roy. Meteor. Soc.*, **141**, 2350–2375, doi:10.1002/qj.2528.

Hosoda, S., T. Ohira, K. Sato, and T. Suga, 2010: Improved description of global mixed-layer depth using Argo profiling floats. *J. Oceanogr.*, **66**, 773–787, doi:10.1007/s10872-010-0063-3.

Huffman, G. J., and Coauthors, 1997: The Global Precipitation Climatology Project (GPCP) combined precipitation dataset. *Bull. Amer. Meteor. Soc.*, **78**, 5–20, doi:10.1175/1520-0477(1997)078<0005:TGPCPG>2.0.CO;2.

——, R. F. Adler, D. T. Bolvin, G. Gu, 2009: Improving the global precipitation record: GPCP version 2.1. *Geophys. Res. Lett.*, **36**, L17808, doi:10.1029/2009GL040000.

Janowiak, J. E., A. Gruber, C. R. Kondragunta, R. E. Livezey, and G. J. Huffman, 1998: A comparison of the NCEP–NCAR reanalysis precipitation and the GPCP rain gauge-satellite combined dataset with observational error considerations. *J. Climate*, **11**, 2960–2979, doi:10.1175/1520-0442(1998)011<2960:ACOTNN>2.0.CO;2.

Jin, X., and L. Yu, 2013: Assessing high-resolution analysis of surface heat fluxes in the Gulf Stream region. *J. Geophys. Res. Oceans*, **118**, 5353–5375, doi:10.1002/jgrc.20386.

——, ——, D. L. Jackson, and G. A. Wick, 2015: An improved near-surface specific humidity and air temperature climatology for the SSM/I satellite period. *J. Atmos. Oceanic Technol.*, **32**, 412–433, doi:10.1175/JTECH-D-14-00080.1.

Josey, S. A., L. Yu, S. Gulev, X. Jin, N. Tilinina, B. Barnier, and L. Brodeau, 2014: Unexpected impacts of the tropical Pacific array on reanalysis surface meteorology and heat fluxes. *Geophys. Res. Lett.*, **41**, 6213–6220, doi:10.1002/2014GL061302.

Kalnay, E., and Coauthors, 1996: The NCEP/NCAR 40-Year Reanalysis Project. *Bull. Amer. Meteor. Soc.*, **77**, 437–471, doi:10.1175/1520-0477(1996)077<0437:TNYRP>2.0.CO;2.

Kanamitsu, M., W. Ebisuzaki, J. Woollen, S.-K. Yang, J. J. Hnilo, M. Fiorino, and G. L. Potter, 2002: NCEP–DOE AMIP-II Reanalysis (R-2). *Bull. Amer. Meteor. Soc.*, **83**, 1631–1643, doi:10.1175/BAMS-83-11-1631.

Kobayashi, S., and Coauthors, 2015: The JRA-55 Reanalysis: General specifications and basic characteristics. *J. Meteor. Soc. Japan*, **93**, 5–48, doi:10.2151/jmsj.2015-001.

Kumar, A., and Z. Hu, 2012: Uncertainty in the ocean–atmosphere feedbacks associated with ENSO in the reanalysis products. *Climate Dyn.*, **39**, 575–588, doi:10.1007/s00382-011-1104-3.

——, F. Yang, L. Goddard, and S. Schubert, 2004: Differing trends in the tropical surface temperatures and precipitation over land and oceans. *J. Climate*, **17**, 653–664, doi:10.1175/1520-0442(2004)017<0653:DTITTS>2.0.CO;2.

Lagerloef, G., and Coauthors, 2008: The Aquarius/SAC-D Mission: Designed to meet the salinity remote-sensing challenge. *Oceanography*, **21**, 68–81, doi:10.5670/oceanog.2008.68.

Lee, T., 2016: Consistency of Aquarius sea surface salinity with Argo products on various spatial and temporal scales. *Geophys. Res. Lett.*, **43**, 3857–3864, doi:10.1002/2016GL068822.

Lorenz, C., and H. Kunstmann, 2012: The hydrological cycle in three state-of-the-art reanalyses: Intercomparison and performance analysis. *J. Hydrometeor.*, **13**, 1397–1420, doi:10.1175/JHM-D-11-088.1.

Lukas, R., and E. Lindstrom, 1991: The mixed layer of the western equatorial Pacific Ocean. *J. Geophys. Res.*, **96**, 3343–3357, doi:10.1029/90JC01951.

Mignot, J., and C. Frankignoul, 2003: On the interannual variability of surface salinity in the Atlantic. *Climate Dyn.*, **20**, 555–565, doi:10.1007/s00382-002-0294-0.

Molod, A., L. Takacs, M. Suarez, and J. Bacmeister, 2015: Development of the GEOS-5 atmospheric general circulation model: Evolution from MERRA to MERRA2. *Geosci. Model Dev.*, **8**, 1339–1356, doi:10.5194/gmd-8-1339-2015.

Mueller, B., and Coauthors, 2013: Benchmark products for land evapotranspiration: LandFlux-EVAL multi-data set synthesis. *Hydrol. Earth Syst. Sci.*, **17**, 3707–3720, doi:10.5194/hess-17-3707-2013.

Newman, M., P. D. Sardeshmukh, and J. W. Bergman, 2000: An assessment of the NCEP, NASA, and ECMWF reanalyses over the tropical west Pacific warm pool. *Bull. Amer. Meteor. Soc.*, **81**, 41–48, doi:10.1175/1520-0477(2000)081<0041:AAOTNN>2.3.CO;2.

Poli, P., and Coauthors, 2013: The data assimilation system and initial performance evaluation of the ECMWF pilot reanalysis of the

20th-century assimilating surface observations only (ERA-20C). ERA Rep. Series, Vol. 14, 59 pp. [Available online at http://www.ecmwf.int/en/elibrary/11699-data-assimilation-system-and-initial-performance-evaluation-ecmwf-pilot-reanalysis.]

Quartly, G. D., E. A. Kyte, M. A. Srokosz, and M. N. Tsimplis, 2007: An intercomparison of global oceanic precipitation climatologies. *J. Geophys. Res.*, **112**, D10121, doi:10.1029/2006JD007810.

Ren, L., E. Hackert, P. Arkin, and A. J. Busalacchi, 2014: Estimating the global oceanic net freshwater flux from Argo and comparing it with satellite-based freshwater flux products. *J. Geophys. Res. Oceans*, **119**, 7869–7881, doi:10.1002/2013JC009620.

Reynolds, R. W., T. M. Smith, C. Liu, D. B. Chelton, K. S. Casey, and M. G. Schlax, 2007: Daily high-resolution-blended analyses for sea surface temperature. *J. Climate*, **20**, 5473–5496, doi:10.1175/2007JCLI1824.1.

Rhein, M., and Coauthors, 2013: Observations: Ocean. *Climate Change 2013: The Physical Science Basis*, T. F. Stocker et al., Eds., Cambridge University Press, 255–315, doi:10.1017/CBO9781107415324.010.

Rienecker, M. M., and Coauthors, 2011: MERRA: NASA's Modern-Era Retrospective Analysis for Research and Applications. *J. Climate*, **24**, 3624–3648, doi:10.1175/JCLI-D-11-00015.1.

Roads, J., 2003: The NCEP–NCAR, NCEP–DOE, and TRMM tropical atmosphere hydrologic cycles. *J. Hydrometeor.*, **4**, 826–840, doi:10.1175/1525-7541(2003)004<0826:TNNATT>2.0.CO;2.

Robertson, F. R., M. G. Bosilovich, J. B. Roberts, R. H. Reichle, R. Adler, L. Ricciardulli, W. Berg, and G. J. Huffman, 2014: Consistency of estimated global water cycle variations over the satellite era. *J. Climate*, **27**, 6135–6154, doi:10.1175/JCLI-D-13-00384.1.

Rosenfeld, D., and I. M. Lensky, 1998: Satellite-based insights into precipitation formation processes in continental and maritime convective clouds. *Bull. Amer. Meteor. Soc.*, **79**, 2457–2476, doi:10.1175/1520-0477(1998)079<2457:SBIIPF>2.0.CO;2.

Saha, S., and Coauthors, 2010: The NCEP Climate Forecast System Reanalysis. *Bull. Amer. Meteor. Soc.*, **91**, 1015–1057, doi:10.1175/2010BAMS3001.1.

Schanze, J. J., R. W. Schmitt, and L. Yu, 2010: The global oceanic freshwater cycle: A state-of-the-art quantification. *J. Mar. Res.*, **68**, 569–595, doi:10.1357/002224010794657164.

Schlosser, C. A., and P. R. Houser, 2007: Assessing a satellite-era perspective of the global water cycle. *J. Climate*, **20**, 1316–1338, doi:10.1175/JCLI4057.1.

Schneider, T., T. Bischoff, and G. H. Haug, 2014: Migrations and dynamics of the intertropical convergence zone. *Nature*, **513**, 45–53, doi:10.1038/nature13636.

Tang, W., S. H. Yueh, A. G. Fore, A. Hayashi, T. Lee, and G. Lagerloef, 2014: Uncertainty of Aquarius sea surface salinity retrieved under rainy conditions and its implication on the water cycle study. *J. Geophys. Res. Oceans*, **119**, 4821–4839, doi:10.1002/2014JC009834.

Taylor, P. K., E. F. Bradley, C. W. Fairall, L. Legler, J. Schulz, R. A. Weller, and G. H. White, 1999: Surface fluxes and surface reference sites. *Proc. OceanObs'99*, St Raphael, France, OceanSITES, 29 pp. [Available online at http://www.oceansites.org/docs/OceanObs99SurfFluxes.pdf.]

Terray, L., L. Corre, S. Cravatte, T. Delcroix, G. Reverdin, and A. Ribes, 2012: Near-surface salinity as Nature's rain gauge to detect human influence on the tropical water cycle. *J. Climate*, **25**, 958–977, doi:10.1175/JCLI-D-10-05025.1.

Trenberth, K. E., and J. G. Olson, 1988: An evaluation and intercomparison of global analyses from the National Meteorological Center and the European Centre for Medium-Range Weather Forecasts. *Bull. Amer. Meteor. Soc.*, **69**, 1047–1057, doi:10.1175/1520-0477(1988)069<1047:AEAIOG>2.0.CO;2.

——, and L. Smith, 2005: The mass of the atmosphere: A constraint on global analyses. *J. Climate*, **18**, 864–875, doi:10.1175/JCLI-3299.1.

——, J. M. Caron, and D. P. Stepaniak, 2001: The atmospheric energy budget and implications for surface fluxes and ocean heat transports. *Climate Dyn.*, **17**, 259–276, doi:10.1007/PL00007927.

——, L. Smith, T. Qian, A. Dai, and J. Fasullo, 2007: Estimates of the global water budget and its annual cycle using observational and model data. *J. Hydrometeor.*, **8**, 758–769, doi:10.1175/JHM600.1.

——, J. T. Fasullo, and J. Mackaro, 2011: Atmospheric moisture transports from ocean to land and global energy flows in reanalyses. *J. Climate*, **24**, 4907–4924, doi:10.1175/2011JCLI4171.1.

Uppala, S. M., and Coauthors, 2005: The ERA-40 Re-Analysis. *Quart. J. Roy. Meteor. Soc.*, **131**, 2961–3012, doi:10.1256/qj.04.176.

van der Ent, R. J., and H. H. G. Savenije, 2013: Oceanic sources of continental precipitation and the correlation with sea surface temperature. *Water Resour. Res.*, **49**, 3993–4004, doi:10.1002/wrcr.20296.

Vinogradova, N. T., and R. M. Ponte, 2013: Clarifying the link between surface salinity and freshwater fluxes on monthly to interannual time scales. *J. Geophys. Res. Oceans*, **118**, 3190–3201, doi:10.1002/jgrc.20200.

Wang, B., and Q. Ding, 2008: Global monsoon: Dominant mode of annual variation in the tropics. *Dyn. Atmos. Oceans*, **44**, 165–183, doi:10.1016/j.dynatmoce.2007.05.002.

Wen, C., Y. Xue, and A. Kumar, 2012: Ocean–atmosphere characteristics of tropical instability waves simulated in the NCEP Climate Forecast System Reanalysis. *J. Climate*, **25**, 6409–6425, doi:10.1175/JCLI-D-11-00477.1.

Xie, P., and P. A. Arkin, 1997: Global precipitation: A 17-year monthly analysis based on gauge observations, satellite estimates, and numerical model outputs. *Bull. Amer. Meteor. Soc.*, **78**, 2539–2558, doi:10.1175/1520-0477(1997)078<2539:GPAYMA>2.0.CO;2.

Yin, X., A. Gruber, and P. Arkin, 2004: Comparison of the GPCP and CMAP merged gauge–satellite monthly precipitation products for the period 1979–2001. *J. Hydrometeor.*, **5**, 1207–1222, doi:10.1175/JHM-392.1.

Yu, L., 2011: A global relationship between the ocean water cycle and near-surface salinity. *J. Geophys. Res.*, **116**, C10025, doi:10.1029/2010JC006937 .

——, 2014: Coherent evidence from Aquarius and Argo on the existence of a shallow low-salinity convergence zone beneath the Pacific ITCZ. *J. Geophys. Res. Oceans*, **119**, 7625–7644, doi:10.1002/2014JC010030.

——, 2015: Sea-surface salinity fronts and associated salinity-minimum zones in the tropical ocean. *J. Geophys. Res. Oceans*, **120**, 4205–4225, doi:10.1002/2015JC010790.

——, and R. A. Weller, 2007: Objectively Analyzed Air–Sea Heat Fluxes (OAFlux) for the global ice-free oceans (1981–2005). *Bull. Amer. Meteor. Soc.*, **88**, 527–539, doi:10.1175/BAMS-88-4-527.

——, and X. Jin, 2014a: Insights on the OAFlux ocean surface vector wind analysis merged from scatterometers

and passive microwave radiometers (1987 onward). *J. Geophys. Res. Oceans*, **119**, 5244–5269, doi:10.1002/2013JC009648.

——, and ——, 2014b: Confidence and sensitivity study of the OAFlux multisensor synthesis of the global ocean surface vector wind from 1987 onward. *J. Geophys. Res. Oceans*, **119**, 6842–6862, doi:10.1002/2014JC010194.

——, ——, and R. A. Weller, 2008: Multidecade Global Flux Datasets from the Objectively Analyzed Air–Sea Fluxes (OAFlux) Project: Latent and sensible heat fluxes, ocean evaporation, and related surface meteorological variables. Woods Hole Oceanographic Institution, OAFlux Project Tech. Rep. OA-2008-01, 64 pp.

Yueh, S., W. Tang, A. Fore, A. Hayashi, Y. T. Song, and G. Lagerloef, 2014: Aquarius geophysical model function and combined active passive algorithm for ocean surface salinity and wind retrieval. *J. Geophys. Res. Oceans*, **119**, 5360–5379, doi:10.1002/2014JC009939.

Zhang, L., A. Kumar, and W. Wang, 2012: Influence of changes in observations on precipitation: A case study for the Climate Forecast System Reanalysis (CFSR). *J. Geophys. Res.*, **117**, D08105, doi:10.1029/2011JD017347.